SLAC-PUB-1116
(EXP) and (EXPI)
September 1972

PERFORMANCE OF THE SLAC 2-METER STREAMER CHAMBER IN A STUDY OF MULTIBODY PHOTOPRODUCTION*

D. C. Fries,** M. Davier, I. Derado,***
F. F. Liu,† R. F. Mozley, A. C. Odian,
J. Park,*** W. P. Swanson,
F. Villa, and D. Yount††

Stanford Linear Accelerator Center
Stanford University, Stanford, California 94305

(Submitted to Nucl. Instr. and Methods.)

---

*Work supported by the U. S. Atomic Energy Commission.

**Institut für Experimentale Kernphysik, Universität Karlsruhe, Karlsruhe, Germany.

***Max-Planck-Institut für Physik and Astrophysik, Munich, Germany.

†Physics Department, California State College, San Bernardino, California 92407, U. S. A.

††Department of Physics and Astronomy, University of Hawaii, Honolulu, Hawaii 96822, U. S. A.

ABSTRACT

The performance of the SLAC 2-meter streamer chamber is evaluated using the results of a high-statistics, multibody-photoproduction experiment carried out with an 18 GeV bremsstrahlung beam. The instrumental arrangement is outlined, and the data-analysis procedures are described in detail. Special methods are then discussed for dealing with trigger, dip-angle, and hydrogen-target losses and for weighting the surviving events. Finally, the spatial resolution, instrumental efficiency, and overall normalization accuracy are given, and the momentum range over which particle types can be distinguished by ionization is specified. The results of this evaluation indicate that the streamer chamber is successful in combining the high geometrical resolution, excellent multiple-track efficiency, nearly 4π solid angle, and ionization capabilities of the bubble chamber with the high repetition rate and triggering facility of the spark chamber.

I. INTRODUCTION

During the last decade, a considerable effort has been made to develop an instrument that incorporates the isotropy, the high multiple-track efficiency, and the high resolution of the bubble chamber with the triggering capability of the spark chamber. The first step, the wide-gap spark chamber, was reported by A. I. Alikhanian and his collaborators in 1963.[1] The successful operation of the first streamer chamber was announced by G. E. Chikovani and his co-workers several months later.[2] Streamer-chamber work at SLAC dates from these early reports and led to the 2-meter streamer chamber in 1967.[3,4]

While the technical development of the 2-meter streamer chamber has been reviewed in detail in an unpublished SLAC report,[4] its subsequent performance has been discussed only briefly in publications of experimental results.[5,6] In this report, the performance per se of the 2-meter streamer chamber is evaluated using data from a multibody photoproduction experiment[6] in which 39 000 events were analyzed. The high statistics of this application made it possible and necessary to study trigger efficiencies and scanning biases thoroughly and to develop appropriate techniques for this purpose. The programs used for geometric and kinematic reconstruction are also discussed here, since they differ from those used in bubble-chamber analysis, owing to the lack of a visible primary vertex and to the use of a nonuniform magnetic field. The reconstruction accuracy and inherent limitations of this technique are then given.

II. EXPERIMENTAL APPARATUS

The experimental arrangement is shown in side view in Fig. 1 and in top view in Fig. 2. An 18 GeV bremsstrahlung beam was incident from the left. This photon beam was produced by directing an 18 GeV electron beam with

10^{-5} radian-cm phase space and with $\Delta p/p \sim 1\%$, onto a 1-mm-diameter, 0.25-mm-thick aluminum radiator. A 1.0-mm-diameter source collimator and a lithium-hydride beam hardener in a magnetic field were located downstream of the radiator and were followed by a 1.0-mm-diameter defining collimator 47 m from the radiator, as well as by several scraping collimators at intervals covering an additional 50 m. This configuration resulted in a halo-free beam 3 mm in diameter at the streamer chamber. The photon beam traversed the streamer chamber within a Mylar tube 2.2 m long that contained hydrogen gas at a nominal pressure of 8 atm. The Mylar tube was 1.25 cm in diameter with a wall thickness of 0.1 mm.

After passing through the hydrogen target and streamer chamber, the photon beam continued downstream until it stopped in a quantameter with a standard 95% Argon-5% CO_2 gas filling. The quantameter served to monitor the photon beam intensity and has been calibrated to better than $\pm 1\%$ relative to the SLAC Faraday cup using incident positrons and electrons.[7] The quantameter was operated at ambient temperature and pressure, which were continuously recorded. The net effects of changes in these quantities and of quantameter drift were less than $\pm 0.4\%$. The beam was also monitored by a scintillation counter in order to maintain a uniform time structure. The beam was shut off during the dead time of the streamer chamber.

The streamer chamber, shown in Figs. 1 and 2, was mounted in the gap of a 450-ton, 6-MW magnet designed to allow access from all sides. The central high-field region was 2.0 m in diameter and 1.0 m high. The magnet was designed for 16 kG operation but was run at 10.4 kG because of power supply limitations at the time of the experiment.

Trigger counters were located in two sets, one above and the other below the median plane, with a 30 cm gap between. A triple coincidence of either the upper or the lower set of counters caused the chamber to fire. The counters were spaced in front of, inside of, and behind a conventional high-Z spark chamber used to detect γ rays from π^0 decays. The 30 cm gap was left in the central plane in order to avoid triggering by $e^{\pm}$ pairs. However, an additional set of smaller counters was placed downstream in the central plane of this gap to detect high-energy, small-angle pions and thus to improve the triggering efficiency at high energies. These "slot" counters were shielded by 40 radiation lengths of lead, which allowed an average detection efficiency of 34% for pions above 4 GeV/c, while attenuating $e^{\pm}$ by about a factor of 100.

The streamer chamber was constructed as a rectangular transmission line with a central, planar high-voltage electrode, as shown in Fig. 1. The electrodes were spaced 30 cm apart and were pulsed with a 600 kV, 15 nsec pulse, about 600 nsec after the beam pulse. The drive units, consisting of a Marx generator and a pulse-shaping transmission line (Blumlein), fed the chamber from the left, as can be seen in Figs. 1 and 2. The 22 ohm terminating resistors were on the right. Foam enclosures having upper and lower windows of 0.05 mm laminated Mylar were placed between these electrodes and were filled with 90% Ne-10% He gas at atmospheric pressure. In this experiment, the electrodes were outside the sensitive Ne-He volume, but subsequently it was found preferable to have the wire and metal electrodes inside of the Ne-He gas so that the Mylar windows were in the zero-electric-field region outside of the electrode structure.[8] This change was motivated by the observation that tracks close to the windows could be distorted by any surface charge remaining on the Mylar.

Methods of producing a satisfactory high-voltage pulse are described in detail in Ref. 4. When such a pulse is applied to the Ne-He chamber gas immediately following the passage of a charged particle, Townsend avalanches begin to form along the ionization path. When the electron density in the avalanche head is sufficiently high, photoionization becomes the dominant process, and a symmetric development, called streamer formation, occurs at both ends of each avalanche. If the electric field is strong enough ($\sim$ 20 kV/cm) and of sufficiently short duration ($\sim$ 15 nsec), the individual streamers will be approximately 1 mm in diameter and will grow to a length of less than 1 cm. Such streamers produce enough light to be directly photographed.

The streamer chamber was viewed through the open center of the upper magnet coil by three cameras mounted on top of the magnet, as is also shown in Figs. 1 and 2. Streamer tracks were thus seen through the Mylar windows of the Ne-He cells and through the chamber electrodes, which in the viewing region consisted of planes of parallel 0.25-mm-diameter wires spaced 5 mm apart. The camera axes were vertical. Zeiss Planar (f/1.4) lenses were used with a demagnification in the central plane of 70. This choice was dictated by the availability of otherwise suitable cameras having a 35 mm film format. Kodak film (SO 265) was used, and during most of the experiment, pictures were taken at f/1.4, although operation at up to f/2.4 was later found to be feasible with higher chamber voltages.

Every 16th photograph of the chamber was taken with a timed, rather than a triggered pulse. These photographs contained a random sample of $e^{\pm}$ pairs that were used to determine the incident bremsstrahlung spectrum. A supplementary calibration of the beam intensity was also obtained from these photographs by means of a positron count described later.

The high-Z spark chamber down beam of the streamer chamber was operated during about half of the 18 GeV experiment. The high-Z chamber consisted of 20 modular, double-gap chambers with 2.5 cm gaps and an electrode area 2 m by 1 m. The three electrodes of each module were constructed of 1.9-cm-thick foam with aluminum sheets on either side. The edges of the Ne-He volume were defined by lucite window frames 0.6 cm thick. Ten such modules were hung above, and 10 more below, the central plane, and a total of 10 radiation lengths of lead in thin sheets was suspended between successive modules beginning after module 2 and ending just upstream of module 10. The modules were essentially parallel, and glass prisms were used to direct the light toward two cameras located above the modular array.

III. DATA ANALYSIS

A. Scanning and Measuring

About 600 000 pictures were taken in three views, and they were evaluated in a manner similar to that used in bubble chamber experiments. A 3-prong event is shown in Fig. 3. The film was independently scanned twice in a routine way and was scanned a third time by more experienced scanners to resolve discrepancies. Measurements were carried out on two types of hand-guided machines, a film-plane digitizer of 1.0-μ least count (NRI), and an image-plane digitizer of 2.6-μ least count on film (SPVB).

A special problem in this analysis was the presence of occasional flares, obscured areas of varying size, caused by abnormally strong electric discharges. These flares were frequently associated with tracks at large angles to the electrodes or with tightly spiraling δ-rays. They led to difficulties in interpretation and measurement in a small, but not negligible fraction of the events, and they gave rise to a dip-angle-dependent bias in the raw data sample.

Corrections for these effects were made in a manner to be described later. In subsequent development, the addition of a low-ionization-potential gas ($\frac{1}{4}$% isobutane) reduced the number of flares noticeably and their average diameter by about a third.

B. Chamber Optics and Magnetic Field

The three streamer chamber cameras were located 4.02 m above the central plane of the chamber and placed at the vertices of an isosceles triangle of base 1.2 m and height 1.0 m, as indicated in Figs. 1 and 2. The mean demagnification was 70. The lens distortions were appreciable at large angles and resulted in radial displacements as large as 4.5 cm at a viewing angle of 21° from the optic axis. A radial correction of the form

$$R' = R(1 + \alpha \tan^2 \Theta + \beta \tan^4 \Theta)^{-1} \qquad (1)$$

was introduced in each view, where R, R' are the measured and corrected radial distances from the optic axis, Θ is the corresponding polar angle, α is approximately -0.02, and β was set to zero.[9] Precise values of the optical parameters, including the distortion constant α, were obtained by a least-squares fit using 25 bottom and 2 top fiducials, which were reconstructed in space with an average error of 300 μ. No significant tilt of the film planes was detected.

The three components of the magnetic field were measured by integrating the flux lines through three small coils having orthogonal axes aligned with the respective Cartesian coordinates of the chamber. The coils were mounted on a carriage which was moved in 5 cm steps along parallel lines in 8 horizontal planes. This field mapping extended well into the fringe-field region and yielded a mesh of 30 000 measurements for each component. These relative

data points were then normalized to absolute measurements of the field made along the vertical symmetry axis of the magnet with a nuclear magnetic resonance (NMR) probe.

The field strength in the center of the magnet gap was $B_z = 10.35$ kG with a radial component reaching about 30% of B_z within the visible region of the chamber. The accuracy of the field measurements was estimated to be better than ±20 G. Figure 4 shows representative field profiles taken at different heights above the pole.

The field was assumed to be cylindrically symmetric and was represented by a different pair of functions, $B_z(r,z)$ and $B_r(r,z)$, in each of three radial regions. These functions were polynomials or inverse polynomials (for rapidly varying regions) of the general form

$$B_z(r,z) = \sum_n a_n(z)\, r^n \qquad \text{or} \qquad \left[\sum_n b_n(z)\, r^n\right]^{-1} \tag{2a}$$

$$B_r(r,z) = \sum_n c_n(z)\, r^n \qquad \text{or} \qquad \left[\sum_n d_n(z)\, r^n\right]^{-1} \tag{2b}$$

where a_n, b_n, c_n, and d_n are polynomials in z. A total of 100 coefficients was needed to represent the field to within ±30 G of the measured values in a volume of roughly $4.2 \times 2.0 \times 0.8$ m^3.

C. Geometric Reconstruction

Since the vertex region was obscured by the hydrogen target tube (Fig. 3), tracks associated with a particular vertex were fitted simultaneously, including the vertex coordinates. This approach is different from that normally used in bubble chamber analysis, where events are reconstructed track-by-track with subsequent extrapolations to a common vertex. Similarly, the rapid variation of the magnetic field, even in the chamber region, meant that the tracks could

not be adequately represented by an analytic expression, such as a helix, as is usually possible in bubble-chamber work. Instead, the equation of motion for each charged particle was integrated directly using a Runge-Kutta method. These special features were incorporated in a new geometry program, SYBIL,[10] which was used to reconstruct the events.

In Fig. 5 the root-mean-square deviations on the film plane are given in microns for the reconstructed tracks from 4000 $\gamma p \rightarrow p\pi^+\pi^-$ events. The events shown were measured on the SPVB with about 6-9 points for each track and an average length of 70 cm in space. The distribution shown has a mode or most probable value of 6.5 μ and a full width at half maximum of 5 μ. The deviations obtained by different measurers ranged from a mode of 5 μ with 4-μ width to a mode of 8 μ with a 6-μ width. This lead us to believe that these RMS deviations are mainly attributable to human setting error.

Figure 6 shows the invariant-mass distribution of pion pairs calculated from the measured values of the track momenta in the decay $K^o \rightarrow \pi^+\pi^-$. This sample of V events had an average track length of about 70 cm and an average momentum of 3 GeV/c. A Gaussian fit to these data yields a mean mass for the K^o of (498.7±0.4) MeV with a standard deviation of (5.7±0.5) MeV. This compares well with the accepted mass of 497.87 MeV.[11]

The distribution of the squared photon mass M_γ^2 in the reaction $\gamma p \rightarrow p\pi^+\pi^-$ is shown in Fig. 7. The mass-squared values were computed from the measured values of the outgoing track parameters. The distribution for all photon energies is well centered and symmetric about zero photon mass. The mass resolution indicated by the half width at half maximum is 0.02 GeV^2 averaged over all energies. This number is, of course, energy dependent and varied in our experiment from less than 0.02 GeV^2 for low energy events with $E_\gamma < 5.5$ GeV (which dominate this distribution) to 0.03 GeV^2 for the photon

interval $5.5 < E_\gamma < 7$ GeV and 0.09 GeV^2 for the interval $12 < E_\gamma < 18$ GeV. The mass resolution at low energy was somewhat better than that of an 80-cm bubble chamber for the same reaction.[12] This is not surprising since multiple scattering, which is significant in bubble chambers, is negligible in the streamer chamber case.

D. Kinematic Fitting

The kinematic analysis was carried out using the program FIT70,[13] which took into account the full covariance matrix of SYBIL, including elements correlating different tracks. Although the energy of each photon was not known a priori, the beam was narrowly collimated and its direction well defined. Consequently, an event for which all outgoing particles were measured yielded a three-constraint (3C) fit. In FIT70 each 3C fit was preceded by a preliminary 2C fit in which only momentum conservation, i.e., transverse momentum balance, was required. A conservative χ^2-cut was then employed to eliminate events with unseen particles.

For events passing the above test for no missing neutrals, the solutions of the preliminary 2C fit were such that the final 3C fit, including the energy constraint, required only a few steps to converge. Particular care was taken in FIT70 that all events did, in fact, converge to a minimum χ^2 rather than fail for some technical reason. In the sample of about 200 000 fits, less than 0.05% failed to converge.

As previously shown (Fig. 5), the root-mean-square deviation of points from the reconstructed tracks (the RMS setting error) was about 6.5 μ on film. As the tracks had an average of 25 measured points for all 3 views, the uncertainty in reconstructed track parameters arising from random measurement errors was reduced to the point where systematic errors inherent in the

entire experimental system might dominate. These effects were, in fact, apparent in the χ^2 and stretch distributions after kinematic fitting, which indicated that errors in track parameters as transmitted in the SYBIL error matrix were underestimated.

In order to obtain a reasonably flat χ^2-probability distribution in the kinematic fitting, it was necessary to scale χ^2 by a factor of about $(2.5)^{-2}$ Figure 8 shows this distribution (after scaling) for a sample of 5962 $\gamma p \rightarrow p\pi^+\pi^-$ events averaged over all photon energies $3.5 < E_\gamma < 18$ GeV. The required scaling factor provided us with an estimate of the total effective systematic error inherent in the entire experimental system of $\pm 6\ \mu$, or about $\pm 400\ \mu$ in space. A large part of this uncertainty is associated with systematic errors in the photography and analysis processes, which by themselves contributed $\pm 300\ \mu$ in space (see Section IIIB).

The stretch S(x) for a given track parameter is defined to be

$$S(x) = \frac{x^m - x^f}{(<\delta x^m\, \delta x^m> - <\delta x^f\, \delta x^f>)^{1/2}} \quad , \tag{3}$$

where x refers to one of the track variables 1/p, λ, or ϕ, and where δx is the corresponding error. The superscript m refers to "measured" quantities (SYBIL output), while f refers to the corresponding result after the kinematic fit. The S(x) distribution is a Gaussian with unit standard deviation centered at zero. Symmetry about zero can be taken as evidence that no serious errors were present in the reconstruction parameters, magnetic field, or beam direction. Figure 9 shows the stretch distributions for π^- in the reaction $\gamma p \rightarrow p\pi^+\pi^-$. The 1/p and ϕ distributions are centered and symmetric about

zero, and the λ distribution is shifted slightly, possibly due to a small error ($\sim 0.1 - 0.2$ mrad) in beam direction. All distributions are wider than expected by a factor of 2.5 - 3.5, thus reflecting the scaling factor required in χ^2. The corresponding distributions for π^+ and proton are similar to those shown for π^-.

E. Ionization Information

The streamer chamber preserves information on the number of ion pairs per unit path length produced by a charged particle, and hence allows an identification of the particle mass. However, the number of streamers is not in general a linear function of the number of primary ions, since the densely packed streamers tend to coalesce.[4] Nevertheless, the track brightness, whether enhanced by streamer density or by streamer size, does provide a practical measure of the ionization loss and can be used effectively to distinguish particle types.

In this experiment, protons with momenta less than about 1 GeV/c could be recognized on the scanning table by a visual comparison of the brightness of various tracks in the same picture. This facility was confirmed by comparing the accepted mass hypotheses from 3C fits to a large sample of events with the results of visual ionization scans. The unshaded histogram in Fig. 10 shows the projected laboratory-momentum distribution of protons in the reaction $\gamma p \rightarrow p\pi^+\pi^-$ with incident photon energies above 5.5 GeV. The shaded portion of the histogram contains protons positively identified in an ionization scan. For tracks having laboratory momenta less than 1 GeV/c, the proton could be identified 86% of the time.

The apparent track brightness increases when the dip angle is large, not only because of the foreshortening, but also because the streamers are more likely to coalesce. In extreme cases, the track may be observed in the

wide-gap spark, rather than the streamer mode, and the ionization information is then lost. In this experiment, the ionization information was found to be reliable to dip angles as large as 60°, depending on the momentum.

IV. INSTRUMENTAL EFFICIENCY

A. General Considerations

Three major effects were important in determining the overall instrumental efficiency: (1) trigger efficiency, (2) flares causing a variation in efficiency with dip angle, and (3) insensitivity to certain event configurations obscured by the target tube (target efficiency). The first of these was primarily geometrical, depending upon the location of the trigger counters and their response. The material of the high-Z spark chamber introduced additional uncertainties into the trigger efficiency, and special care was taken to evaluate this contribution.

Flares tended to occur whenever a track was produced in the chamber in a direction nearly perpendicular to the electrodes. In such cases, coalescing streamers produced intense wide-gap discharges that were dissipated tangentially at the surfaces of the Mylar windows, obscuring the region nearby. As expected, this effect was most serious for events having tracks at large dip angles $|\lambda|$. Flares were also associated with low-energy δ-rays that generated large numbers of coalescing streamers in helical patterns enclosing the vertical magnetic field lines. In most cases, the event topology could be correctly identified, whether the flares were due to steep event tracks or to accompanying δ-rays. Some identifiable events were, however, lost to the final data base because of difficulties in measurement.

The losses caused by flares were manifest directly in the distribution of tracks as a function of the dip angle. The raw data could thus be used to

derive an appropriate correction factor. The trigger and dip-angle efficiencies were, however, correlated, and the high statistics of this experiment required that special attention be given to the problem of unfolding them. As described later, the events were weighted in a manner that treats both the separate effects and their correlations.

Losses in the target were caused primarily by: (1) low-energy protons that failed to penetrate the target wall with sufficient energy to be measurable and (2) forward high-momentum particles that emerged from the target tube at such great distances from the vertex that they were lost in scanning or were not reliably reconstructed. The momentum cutoff for a proton perpendicularly incident on the 0.1-mm-Mylar target wall was 70 MeV/c, which compares favorably with the cutoff in other types of track chambers. Both mechanisms for losses in the target were dependent upon the event configuration and the energy, and production models were therefore used in making these corrections.

B. Trigger Efficiency

The intrinsic efficiency of the counters was measured under "ideal" conditions and was found to be quite high. For example, the probability of a triple coincidence was 95% for particles having momenta greater than 1.4 GeV/c. In the actual trigger geometry, the efficiency was momentum-dependent and was generally less than "ideal" because of absorption and multiple scattering in the high-Z spark chambers.

The net trigger efficiency was determined empirically by logically grouping the counters into three banks: UP, DOWN, and SLOT, as indicated in Fig. 1 and described in Section II. Secondary tracks of all reconstructed events were extrapolated through the successive counter planes, and those events for which extrapolation showed exactly one hit in each of two counter banks were selected. Such events had

two chances of triggering and were therefore detected with a high trigger efficiency. By comparing the extrapolated hits with the actual counter firings recorded for each trigger on magnetic tape, the probability for missing one of the two tracks could be determined and the efficiency of each counter bank thereby derived. This study was carried out at various particle momenta P, and the results are given as functions of P in Table 1 below.

Table 1

Empirical Counter Efficiencies as Functions of Momentum P

Counter Bank	P < 4 GeV/c	P ≥ 4 GeV/c
UP	$E_U = 0.40 + 0.25\ P - 0.033\ P^2$	$E_U = 0.88$
DOWN	$E_D = 0.40 + 0.20\ P - 0.024\ P^2$	$E_D = 0.82$
SLOT	$E_S = 0.085\ P$	$E_S = 0.34$

Since a large fraction of the events had two or more hits, the average event efficiency was appreciably higher than the numbers in Table 1 suggest. In general, if the ith track of an event hits a trigger bank having an efficiency E_i, the cumulative trigger efficiency is

$$E_T = 1 - \prod_{i=1}^{N} (1-E_i) \quad , \tag{4}$$

where the product contains all tracks that hit a counter bank.

C. Dip-Angle Efficiency

In treating the dip-angle problem, the following assumptions were made:

(1) There was a well defined probability P_i that an event would be lost because of a flare on track i.

(2) The track efficiency, $E_i = 1-P_i$, was a function only of the dip-angle λ_i.

(3) Tracks produced flares independently of one another.

The net dip-angle efficiency for an event with N prongs was then given by the product of the separate track efficiencies,

$$E_{DA} = \prod_{i=1}^{N} E(\lambda_i) \quad . \tag{5}$$

If the variation in triggering efficiency with event configuration is neglected, the intrinsic azimuthal symmetry of the events produced by unpolarized bremsstrahlung can be used to estimate the track efficiency. The geometry is shown in Fig. 11. Since the dip-angle λ coincides with the production polar angle θ in the particular case of tracks originating in the plane containing the beam and the vertical axis ($\psi = \pm 90^{\circ}$, where ψ is the angle of rotation of the track about the beam line), it then suffices to compare the θ distribution for tracks near the vertical beam plane ($\psi \approx \pm 90^{\circ}$) with the θ distribution for tracks near the horizontal beam plane ($\psi \approx 0^{\circ}$ or 180°). The ratio of the two θ distributions gives directly the efficiency as a function of dip angle:

$$E(\lambda) = \frac{N(\theta=\lambda,\ \psi=90^{\circ}\pm 10^{\circ})}{\frac{1}{2}\left[N(\theta=\lambda,\ \psi=0^{\circ}\pm 10^{\circ}) + N(\theta=\lambda,\ \psi=180^{\circ}\pm 10^{\circ})\right]} \quad . \tag{6}$$

Since the trigger efficiency was high ($\langle E_T \rangle \sim 0.9$) for 5-prong events, this event type was used in Eq. (6) to obtain a preliminary estimate of $E(\lambda)$. Even with the high trigger efficiency, however, it was possible that the triggering system, or some other aspect of the experimental arrangement, could have caused distortions in this estimate of $E(\lambda)$. A likely source of such distortions in the azimuthal angular distribution might be, for example, the

SLOT trigger counters, which covered the 30 cm gap between UP and DOWN counter banks with a single-track efficiency of 34% or less.

To check the form of $E(\lambda)$, the azimuthal angular distribution $dN(\theta,\psi)/d\psi$ was first plotted for a particular value of θ. Because of the flare and trigger losses, the raw events with unit weight were nonuniform in ψ. Additional fictitious events were then constructed from the raw data and added to the plot, each with a small weight. This procedure was designed to make the resultant plot uniform in azimuthal angle ψ if the trigger efficiency was given correctly by the results of the preceding section and if the expression for $E(\lambda)$ in Eq. (6) was correct. Fictitious events were constructed from a real event simply by rotating the real event about the beam direction in N_g uniform steps of $360^o/N_g$ each. The weight assigned to step i was then

$$G_i(\psi) = \frac{1 - E_i^{tot}(\psi)}{\sum_{i=1}^{N} E_i^{tot}(\psi)} , \qquad (7)$$

where $E_i^{tot}(\psi)$ is the product $E_T \times E_{DA}$ for that azimuthal step, and E_T and E_{DA} are calculated from Eqs. (4) and (5), respectively.

Equation (7) can be made plausible by imagining that N_p events were produced with a uniform distribution in the azimuthal angle ψ. Assume for simplicity that $E^{tot} = 1.0$ for ψ in the range 0^o to 180^o and that $E^{tot} = 0.0$ for ψ in the range 180^o to 360^o. On the average, $N_p/2$ events will be contained in the raw data sample, and they will be plotted with unit weight in the range 0^o to 180^o. The weights G_i of Eq. (7) will be zero in the range 0^o to 180^o, but in the range from 180^o to 360^o, $(N_p/2) \times (N_g/2)$ fictitious events will be generated, each with weight $G_i = (2/N_g)$. The result is a uniform azimuthal distribution, and this holds true in general, providing E^{tot} is calculated correctly for each step ψ_i.

Since the trigger efficiency E_T was relatively well understood, deviations in $E^{tot} = E_T \times E_{DA}$ could be ascribed to an error in dip-angle efficiency. Thus $E(\lambda)$ could be repeatedly modified and tested using this procedure until a uniform result was obtained. In this experiment the initial form of $E(\lambda)$ given by Eq. (6) and the 5-prong-event sample proved to be satisfactory, but the method did serve as a valuable check. The actual function $E(\lambda)$ used is shown in Fig. 12.

In principle, the dip-angle efficiency could also depend on the momentum and mass of the ionizing particle. For the range of λ where $E(\lambda)$ deviated from unity, however, the majority of the tracks were protons, and it was not feasible to study the momentum dependence. Nor was it possible to analyze pions separately, since they rarely occurred at large $|\lambda|$. The three assumptions at the beginning of this section permit the same $E(\lambda)$ to be used for both the 3-prong and the 5-prong events, and this proved to be a reasonable approximation. The average correction for dip-angle efficiency in this experiment amounted to only 7%, but the foregoing detailed analysis was required to avoid significant angular biases.

Whereas the dip-angle correction was necessitated by flares explicitly associated with steep tracks, the loss of events due to flares on spiraling δ-rays did not depend significantly upon the track angle or the event topology. The δ-ray loss correction was 4.2% as determined by physicists who examined a large number of events that had failed the spatial reconstruction.

D. Weighting of Events

In order to correct for the effects just described, each event was assigned a weight that took into account the trigger efficiency, the dip-angle efficiency, and their correlations. The event symmetry about the beam line was exploited

in a program ISIS,[5c, 14] which performed the following operations:

(1) N_r rotations of each reconstructed event by a random azimuthal angle α_i about the beam direction;

(2) at each α_i, extrapolation of the event tracks through the magnetic field to the trigger counter planes, using the Runge-Kutta method described in Section II;

(3) designation of tracks making the required coincidences as "hits";

(4) calculation of the cumulative trigger efficiency, E_T in Eq. (4), at each α_i;

(5) calculation of the multiplicative dip-angle efficiency, E_{DA} of Eq. (5), at each α_i;

(6) calculation of the total efficiency, $E^{tot}(\alpha_i) = E_T(\alpha_i) \times E_{DA}(\alpha_i)$, at each α_i;

(7) determination of the average detection efficiency, $E_{av} = \frac{1}{N_r} \sum_i E^{tot}(\alpha_i)$, for each event after N_r rotations.

The statistical weight assigned to each event was then $W^{tot} = (E_{av})^{-1}$.

At least 20 rotations N_r were made, and the procedure was terminated when the statistical error in W^{tot} was less than $0.1\, W^{tot}$, or when N_r equalled 50, whichever occurred first. The resulting weights were retained in the event record for subsequent analysis, such as making weighted histograms. The weight distributions were well-behaved in the sense that values near 1.0 occurred frequently and the efficiency improved with increasing prong number. The average weight is shown as a function of the visible energy E_{VIS} in Fig. 13 for 3-prong, 5-prong, 7-prong, and 9-prong events, where

$E_{VIS} \equiv \sum |P_{VIS}|$ is defined to be the sum of the absolute momenta of the visible tracks. It is also given in Table 2 as a percentage correction for $\gamma p \rightarrow p\pi^+\pi^-$ events.

E. Target Efficiency

Effects related to the hydrogen target tube were particularly important for the 3-prong reaction $\gamma p \rightarrow p\pi^+\pi^-$, which is characterized by low-momentum protons and by fast, forward-going pions. This channel will therefore be used to illustrate the correction procedures. Since most protons in this reaction penetrated the target wall at an oblique angle ($<\theta> \sim 75^o$), there was a momentum cutoff of about 70 MeV/c corresponding to the proton range of 0.1 mm Mylar. The minimum four-momentum transfer to the proton, $\Delta^2 \equiv t - t_{min}$, where t_{min} is the kinematic minimum of the four-momentum transfer t, was about $\Delta^2 = 0.007$ $(GeV/c)^2$ for this reaction. Losses were thus neglected above $\Delta^2 = 0.02$ $(GeV/c)^2$, and the observed weighted Δ^2 distribution in the interval 0.02 to 0.4 $(GeV/c)^2$ was fitted to an exponential $A \exp(-B\Delta^2)$ and extrapolated to $\Delta^2 = 0.0$, as illustrated in Fig. 14. The resulting correction for losses at low Δ^2 ranged from 5.2% for $5.5 < E_\gamma < 7$ GeV to 9.4% for $12 < E_\gamma < 18$ GeV. Table 2 summarizes this and other corrections.

The losses associated with high-energy, forward pions hidden by the target tube were clearly evident in distributions of event vertices along the beam direction. Such distributions show a gradual depletion of events downstream, and this loss becomes more pronounced at the higher energies. After the fiducial volume was restricted to a region where the effect was small, a numerical estimate of the loss within this region was obtained by studying the left-right asymmetry in the ϕ distributions for pion tracks. (As shown in

Fig. 11, ϕ is the track angle projected onto the horizontal plane and measured from the beam direction.)

The asymmetry was defined as

$$\alpha^{\pm} = \frac{N(\phi < 0^{o}) - N(\phi > 0^{o})}{N(\phi < 0^{o}) + N(\phi > 0^{o})} \quad , \tag{8a}$$

where N is the number of tracks of the particular type indicated and where the sign refers to the pion charge. The "combined" asymmetry was defined as

$$\alpha = (\alpha^{-} - \alpha^{+})/2 \quad . \tag{8b}$$

Since the π^{+} and π^{-} asymmetries were of similar magnitude and of opposite sign, the "combined" asymmetry is given approximately by

$$\alpha \approx \alpha^{-} \approx -\alpha^{+} . \tag{8c}$$

Thus the magnetic field bent π^{-} to the right ($\phi < 0^{o}$) causing a positive asymmetry $\alpha \approx \alpha^{-} > 0$, while the probability for triggering was higher for π^{-} produced on the left ($\phi < 0^{o}$) leading to a negative asymmetry $\alpha \approx \alpha^{-} < 0$. These two opposing effects can be seen in Fig. 15, where the "combined" asymmetry is plotted versus energy.

The "combined" asymmetry due to the trigger alone α^{trig} was estimated by generating events with the known distributions of invariant mass, momentum transfer, and decay angles. Vertex coordinates and angles about the beam were assigned randomly, and these generated events were then "triggered" by the same configuration of counters and the same efficiencies described earlier. The "combined" trigger asymmetry α^{trig} calculated from this model is also shown in Fig. 15.

Once the trigger asymmetry had been determined, the fractional loss in events due to the target alone was calculated from the ratio $\alpha^{c}/(1+\alpha^{c}-f)$,

where $\alpha^c = \alpha - \alpha^{trig}$ and where f is the fraction of events with both π^+ and π^- tracks on the same side. The correction obtained in this way ranged from 0.0% at $4.5 < E_\gamma < 5.5$ GeV to 8.7% at $12 < E_\gamma < 18$ GeV (Table 2).

V. PHOTON BEAM ANALYSIS

The use of a beam hardener and of stringent collimation resulted in a photon energy distribution somewhat different from the theoretical bremsstrahlung shape. Accordingly, every 16th frame was taken with a timed pulse, rather than a normal triggered pulse, in order to study the beam in an adequate number of photographs not biased by the triggering system.

The timed photographs were first analyzed to give the e^+e^- pair spectrum. The cross section for pair and triplet production was calculated using Wheeler-Lamb screening for hydrogen,[15] and the precise effect of the target tube and the momentum resolution on the observed e^+e^- spectrum was studied by a Monte-Carlo method.[16] Minor corrections were also made for the target tube entrance windows, for the helium gas bag containing the incident beam, and for the small amount of air in the beam path immediately in front of the target entrance.

A supplemental measurement of the photon intensity was made by counting positrons of energy greater than a convenient, but otherwise arbitrary threshold of 42.5 MeV. The e^+ were easily recognizable because of their small production angle, and the contamination by hadronic events was less than 0.1% in the timed photographs. The measured pair spectrum was used to relate the number of e^+ counted to the integrated photon flux, taking into account the aforementioned instrumental effects.

The uncertainty in the measured spectrum shape contributed an energy-dependent uncertainty to the cross section measurements which varied from 0.9% at $5.5 < E_\gamma < 7.0$ GeV/c to 2.6% at $12 < E_\gamma < 18$ GeV (Table 2).

VI. HIGH-Z SPARK CHAMBER ANALYSIS

The tracks of events reconstructed in the streamer chamber were extrapolated through the magnetic fringing field, out to the high-Z spark chamber. Cones containing possible photons from $\pi^o \rightarrow 2\gamma$ decay were also calculated, assuming each event had one missing π^o. A printout was then prepared by the computer for each event showing the paths of all charged particles and the cones within which a photon shower might be visible. These paths were projected in each of the two views of the high-Z chamber and were scaled to the overall magnification used in scanning.

By comparing the actual photographs with the computer printouts, it was possible to identify events of the type $\gamma p \rightarrow p\pi^+\pi^-\pi^o$ with a net efficiency of about 50%. The geometric efficiency was calculated to be 70% by assuming the π^o had the same laboratory angular distributions as the π^+ and π^-. The shower efficiency was estimated also to be about 70% by scanning for charged tracks and by assuming that all photons had the same shower efficiency. The resulting cross sections for channels containing one π^o were consistent with known values at other energies.[17] Scanning for charged tracks in the high-Z chamber also served to test the internal consistency of the analysis programs, including those used in the event-weighting procedures that required extrapolation to the remote counter planes.

The high-Z spark chamber was useful in isolating a relatively pure sample of events containing only one π^o from a severe background of multineutral events, but it decreased the net trigger efficiency of all channels and introduced some uncertainty into the determination of this quantity. Subsequently, it was found that plates of nonconducting high-Z material could be mounted

within the streamer chamber, thereby improving the geometric efficiency while eliminating the need for two extra cameras and the external spark chambers.

VII. SUMMARY OF CORRECTIONS AND ERRORS

The average total correction made to the data amounted to a factor ranging between 2.2 and 2.8, depending upon the bremsstrahlung energy E_γ. The uncertainties in these corrections were a dominant source of experimental error. With corrections of this size, the question also arises of systematic effects on the invariant-mass, the angular, and the momentum-transfer distributions. The most sensitive case was that of the 3-prong, 3C reaction $\gamma p \rightarrow p\pi^+\pi^-$, which is dominated by ρ^0 production. This question was studied by Monte-Carlo calculations using the observed invariant-mass, momentum-transfer, and ρ-decay dependences. A sample was generated and then handled in the same way as the real events. The derived distributions of the quantities studied deviated from the initial distributions by less than the statistical errors. Thus the systematic errors affect primarily the absolute cross-section determinations.

The identified corrections and associated errors are listed in Tables 2 and 3, in which energy-dependent and energy-independent effects are given separately. There is considerable uncertainty in the proper method of combining the estimates of various systematic errors. Tables 2 and 3 (bottom line) give the average of the linear and quadratic sums.

Corrections not previously explained or self-explanatory are described below, where the number indicates the corresponding lines of Tables 2 and 3.

(2f) "Untriggered events" are events that could not have triggered at any azimuthal angle about the beam line. This correction was estimated by plotting the cross section as a function of a

cutoff maximum in the inverse event weight $1/W_{max}$ and by then extrapolating to $1/W_{max} = 0.0$, as illustrated in Fig. 16.

(3c) "Nonanalyzable events" are those found in scanning that failed in reconstruction. Most of the failures resulted from δ-ray-induced flares (4.2%) and from technical defects, such as missing fiducials or defective film (11.6%).

(3d) "Misfiring of chamber" refers to events for which a trigger was produced but the chamber was insensitive, usually because of a substandard high-voltage pulse.

(3e) "Scanning loss" is the estimated fraction of events not found in two scans.

VIII. CONCLUSIONS

The results of this analysis indicate that the streamer chamber is a high resolution track detector that compares favorably with a bubble chamber, while retaining the triggering and high repetition rate capabilities of the spark chamber. There is no particular limit to the volume that can be filled by a streamer chamber, and it is readily adapted to large magnet applications. Like the bubble chamber, the streamer chamber provides a solid angle of nearly 4π, ionization information, high geometrical resolution, and the facility to recognize complicated event topologies. In addition, multiple scattering and energy loss are negligible. In the particular application described here, events occurred inside of a Mylar tube containing pressurized hydrogen gas, and this limited the detection of protons to momenta above 70 MeV/c, comparable with the minimum for bubble chambers. The fact that the event vertices were not measured and that the magnetic field was rather nonuniform

placed no noticeable limit on the resolution of the SLAC 2-meter streamer chamber when compared with other visual techniques.

IX. ACKNOWLEDGEMENTS

We wish to acknowledge the assistance of a large number of persons at SLAC and elsewhere in helping us solve the problems of building and operating the streamer chamber. In particular, we wish to thank the following people who made major contributions to the success of the chamber: R. Bell, R. Ching, D. Danielson, D. Lebet, V. Lee, R. Leedy, E. Maninger, J. McKee, E. McNerney, J. Moss, F. Plunder, T. Pulliam, F. Shuster, G. Schultz, L. Schwarcz, and W. Wadley. We are grateful to our scanning, measuring, and data-analysis staff for their patient work. It is a pleasure to thank the accelerator and computer operating groups and the machine-shop personnel for their assistance.

REFERENCES

1. A. I. Alikhanian, T. L. Asatiani, É. M. Matevosian, and R. O. Sharkhatunyan, Phys. Letters 4, 295 (1963); A. I. Alikhanian, T. L. Asatiani, É. M. Matevosyan, Soviet Phys., JETP 17, 522 (1963); A. I. Alikhanian, Loeb Lecture Notes, Harvard University, Cambridge, Massachusetts (1965) (unpublished).
2. V. A. Mikhaĭlov, V. N. Roĭnishvili, and G. E. Chikovani, Soviet Phys., JETP 18, 561 (1964); G. E. Chikovani, V. N. Roĭnishvili, and V. A. Mikhaĭlov, Soviet Phys., JETP 19, 833 (1964).
3. F. Bulos, "Streamer Wide-Gap Spark Chamber," Report No. SLAC-TN-64-73, Stanford Linear Accelerator Center (1964); F. Bulos, A. Boyarski, R. Diebold, B. Richter, A. Odian, and F. Villa, IEEE Trans. Nucl. Sci. NS-12 (No. 4), 22 (1965); F. Bulos, A. Boyarski, R. Diebold, A. Odian, B. Richter, and F. Villa, "Streamer Chamber Development," Proceedings of the 5th International Conference on High Energy Accelerators, Frascati, Italy, September 9-16, 1965, p. 675; A. Odian, "Streamer Chamber Developments at SLAC," Proceedings of the 1966 International Conference on Instrumentation in High Energy Physics, Stanford Linear Accelerator Center, Stanford, California, September 9-10, 1966, p. 49; F. Villa, "The 2 Meters SLAC Chamber," contribution to the International Symposium on Nuclear Electronics, Versailles, September 10-13, 1968, Documentation Francaise, Paris (1968), p. 7-1.
4. F. Bulos, A. Odian, F. Villa, and D. Yount, "Streamer-Chamber Development," Report No. SLAC-74, Stanford Linear Accelerator Center (1967) (unpublished).

5. First Experiment:

(a) M. Davier, I. Derado, D. Drickey, D. Fries, R. Mozley, A. Odian, F. Villa, D. Yount, and R. Zdanis, Phys. Rev. Letters 21, 841 (1968);

(b) M. Davier, I. Derado, D. Drickey, D. Fries, R. Mozley, A. Odian, F. Villa, and D. Yount, Phys. Letters 28B, 619 (1969);

(c) M. Davier, "Photoproduction des mésons vectoriels entre 2 et 16 GeV," doctoral dissertation, University of Paris (1969);

(d) M. Davier, I. Derado, D. Drickey, D. Fries, R. Mozley, A. Odian, F. Villa, and D. Yount, Phys. Rev. D1, 790 (1970).

6. Second Experiment:

(a) M. Davier, I. Derado, D. C. Fries, F. F. Liu, R. F. Mozley, A. Odian, J. Park, W. P. Swanson, F. Villa, and D. Yount, "Study of the Reaction $\gamma p \rightarrow \pi^+\pi^-\pi^+\pi^- p$ above 4.5 GeV and Evidence for a πA_1 Enhancement," contribution to the International Symposium on Electron and Photon Interactions at High Energies, Daresbury, September, 1969 (Abstract No. 157);

(b) M. Davier, I. Derado, D. C. Fries, F. F. Liu, R. F. Mozley, A. C. Odian, J. Park, W. P. Swanson, F. Villa, and D. Yount, "The Reaction $\gamma p \rightarrow \pi^+\pi^-\pi^+\pi^- p$ at High Energy and Photon Dissociation into 4 Pions," contribution to the International Symposium on Electron and Photon Interactions at High Energies, Cornell University, Ithaca, New York, August 23-27, 1971;

(c) W. P. Swanson, M. Davier, I. Derado, D. C. Fries, F. F. Liu, R. F. Mozley, A. C. Odian, J. Park, F. Villa, and D. E. Yount, Phys. Rev. Letters 27, 1472 (1971);

(d) J. Park, M. Davier, I. Derado, D. C. Fries, F. F. Liu, R. F. Mozley, A. C. Odian, W. P. Swanson, F. Villa, and D. Yount, Nucl. Phys. B36, 404 (1972);

(e) C. Risk, W. P. Swanson, and J. H. Friedman, Nucl. Phys. B43, 178 (1972);

(f) W. P. Swanson, W. Ko, R. L. Lander, C. Risk, R. R. Ross, and D. B. Smith, Phys. Rev. D6, 170 (1972);

(g) F. F. Liu, M. Davier, I. Derado, D. C. Fries, R. F. Mozley, A. C. Odian, J. Park, W. P. Swanson, F. Villa, and D. Yount, "Analysis of γp Reactions in the LPS Framework at E_γ=6-18 GeV," Report No. SLAC-PUB-1057, Stanford Linear Accelerator Center (June 1972) (to be published in Nucl. Phys. B).

This second experiment differs from the first (Ref. 5) in that: (1) the bremsstrahlung energy was 18 rather than 16 GeV; (2) the magnetic field was 10.4 rather than 8.0 kG; (3) an auxiliary high-Z spark chamber was used to detect γ's from π^0 decay; and primarily (4) the number of events was increased 7-fold.

7. D. Yount, Nucl. Instr. and Methods 52, 1 (1967), and Proceedings of the Symposium on Beam Intensity Measurement, Daresbury, England, April, 1968, p. 75.

8. Private communication from DESY streamer chamber group.

9. R. Ching and D. E. Fries, "Determination of the Optical Parameters of the Streamer Chamber Camera System," Report No. SLAC-TN-69-16, Stanford Linear Accelerator Center (1968) (unpublished).

10. D.E.C. Fries, "Filmplane Reconstruction of Trajectories in a Nonuniform Magnetic Field: The Computer Program SYBIL," Report No. SLAC-103, Stanford Linear Accelerator Center (1969) (unpublished). See also I. Derado and D. Fries, Nucl. Instr. and Methods 67, 109 (1969).

11. Particle Data Group, "Review of Particle Properties," Rev. Mod. Phys. 43, S1 (1971).

12. See, for example, H. Spitzer, "Photoproduktion von ρ^0 Mesonen in einer Wasserstoffblasenkammer bei Photonenenergien bis zu 5.8 GeV," doctoral dissertation, Universitat Hamburg, DESY Internal Report F1/4 (1967) (unpublished).

13. J.C.H. Park, "FIT70 - A Kinematic Fitting Routine," Report No. SLAC-150, Stanford Linear Accelerator Center (June, 1972) (unpublished).

14. D.E.C. Fries and W. P. Swanson, SLAC Technical Note, in preparation.

15. J. A. Wheeler and W. E. Lamb, Jr., Phys. Rev. 55, 858 (1939); Phys. Rev. 101, 1836 (1956).

16. D. C. Blanchard and W. P. Swanson, "THEMI - Monte Carlo Generation of Electromagnetic Events," Report No. SLAC-123, Stanford Linear Accelerator Center (1970) (unpublished).

17. J. Ballam, G. B. Chadwick, R. Gearhart, Z.G.T. Guiragossián, J. J. Murray, P. Seyboth, C. K. Sinclair, I. O. Skillicorn, H. Spitzer, G. Wolf, H. H. Bingham, W. B. Fretter, K. C. Moffeit, W. J. Podolsky, M. S. Rabin, A. H. Rosenfeld, R. Windmolders, and R. H. Milburn, Phys. Rev. D5, 545 (1972).

Table 2

Energy-Dependent Corrections and Errors $\gamma p \rightarrow p\pi^+\pi^-$

	Type of Correction	5.5 - 7 GeV Amount Error (per cent)	7 - 9 GeV Amount Error (per cent)	9 - 12 GeV Amount Error (per cent)	12 - 18 GeV Amount Error (per cent)
a.	Spectrum Shape	2.3 ± 0.9	0.6 ± 0.2	1.8 ± 0.8	6.2 ± 2.6
b.	Target Efficiency: Low-Energy Protons	5.2 ± 2.8	2.8 ± 1.3	4.6 ± 1.7	9.4 ± 3.1
c.	Target Efficiency: High-Energy Pions	0.0 ± 2.0	2.4 ± 2.0	5.6 ± 2.0	8.7 ± 2.0
d.	Weighting[(a)]: Trigger Efficiency	34.2 ± 5.0	34.6 ± 5.0	33.8 ± 5.0	36.4 ± 5.0
e.	Weighting[(a)]: Dip-Angle Efficiency				
f.	Untriggered Events	3.7 ± 1.9	2.9 ± 1.5	4.3 ± 2.2	4.7 ± 2.4
	Combined Correction and Error[(b)]	41.1 ± 9.5	40.1 ± 7.9	44.0 ± 8.9	53.0 ± 11.2

(a) Because the two effects corrected in the weighting are correlated, the resultant correction is combined. If considered separately, the dip-angle correction is approximately energy-independent and is about 7.0%.

(b) See text for method used to combine errors.

Table 3

Energy-Independent Corrections and Errors

	Type of Correction	Amount (%)		Error (%)
a.	Equivalent Quanta	0.0	±	1.0
b.	Gas Target Pressure	0.0	±	3.0
c.	Nonanalyzable Events	15.8	±	5.3
d.	Misfiring of Chamber	6.8	±	2.3
e.	Scanning Loss	3.1	±	1.0
Combined Correction and Error[(a)]		24.0	±	9.7

(a) See text for method used to combine errors.

FIGURE CAPTIONS

1. Vertical cross section through the magnet and the streamer chamber.
2. Plan view of the magnet and the streamer chamber.

Photograph of a 3-prong event in the streamer chamber. The gap in the negative track shows the crossing of the particle from the upper into the lower chamber.

4. Magnetic field profiles, where r is the radial distance from the axis of symmetry and z is the height from the bottom pole piece.
5. RMS deviations of measured points from fitted tracks in microns on the film plane.
6. Invariant mass of pion pairs in the decay $K^o \rightarrow \pi^+\pi^-$, calculated from the measured values of the particle momenta.
7. Apparent photon mass squared m_γ^2 for $\gamma p \rightarrow p\pi^+\pi^-$, calculated from the measured values of the particle momenta.
8. χ^2-probability, after scaling, for $\gamma p \rightarrow p\pi^+\pi^-$ events at all photon energies.
9. Stretch distributions (as defined in text) for π^- in $\gamma p \rightarrow p\pi^+\pi^-$.
10. Projected laboratory momentum distribution for outgoing protons in $\gamma p \rightarrow p\pi^+\pi^-$ events with $E_\gamma > 5.5$ GeV. The shaded distribution corresponds to protons positively identified by ionization.
11. Definition of the various angles used in the discussion of the chamber efficiency.
12. Chamber efficiency as a function of dip angle λ.
13. Average event weight for different topologies as a function of the visible energy, where $E_{vis} \equiv \sum |\vec{P}_{vis}|$ is the sum of the absolute momenta of all visible tracks.

14. Proton-proton momentum-transfer distribution (weighted by chamber efficiency) in $\gamma p \rightarrow p\pi^+\pi^-$. The smooth curve shows an exponential fit used to extrapolate to the minimum.

15. Asymmetry (defined in text) in the projected production angle ϕ of pions in $\gamma p \rightarrow p\pi^+\pi^-$.

16. Cross section for $\gamma p \rightarrow p\pi^+\pi^-$ as a function of weight cutoff W_{max}. The smooth curves show extrapolations to no-cutoff.

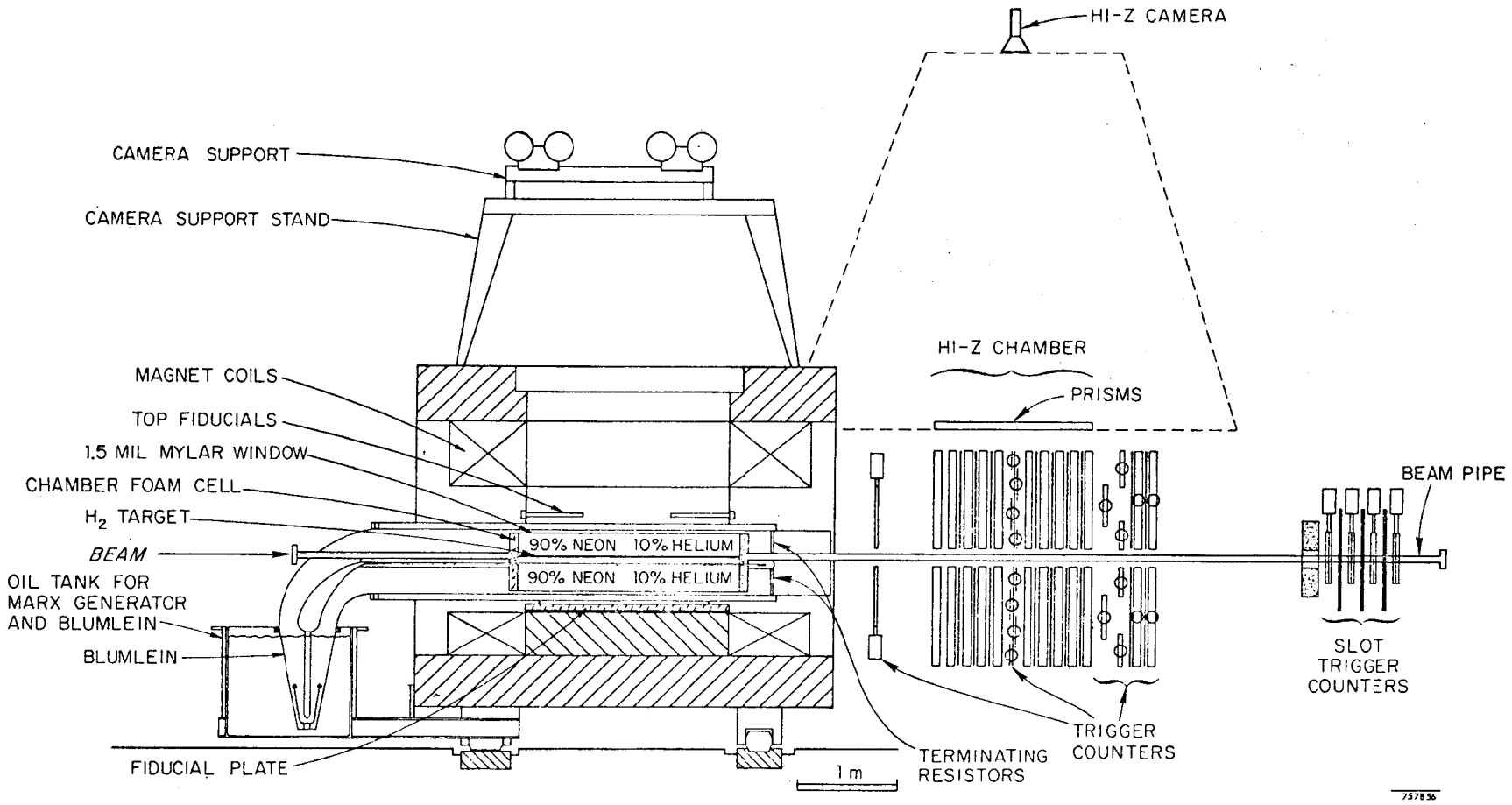
HI-Z CAMERA
CAMERA SUPPORT
CAMERA SUPPORT STAND
HI-Z CHAMBER
PRISMS
MAGNET COILS
TOP FIDUCIALS
1.5 MIL MYLAR WINDOW
CHAMBER FOAM CELL
H_2 TARGET
BEAM
90% NEON 10% HELIUM
90% NEON 10% HELIUM
BEAM PIPE
OIL TANK FOR MARX GENERATOR AND BLUMLEIN
BLUMLEIN
SLOT TRIGGER COUNTERS
TRIGGER COUNTERS
TERMINATING RESISTORS
FIDUCIAL PLATE
1 m
757836

Fig. 1

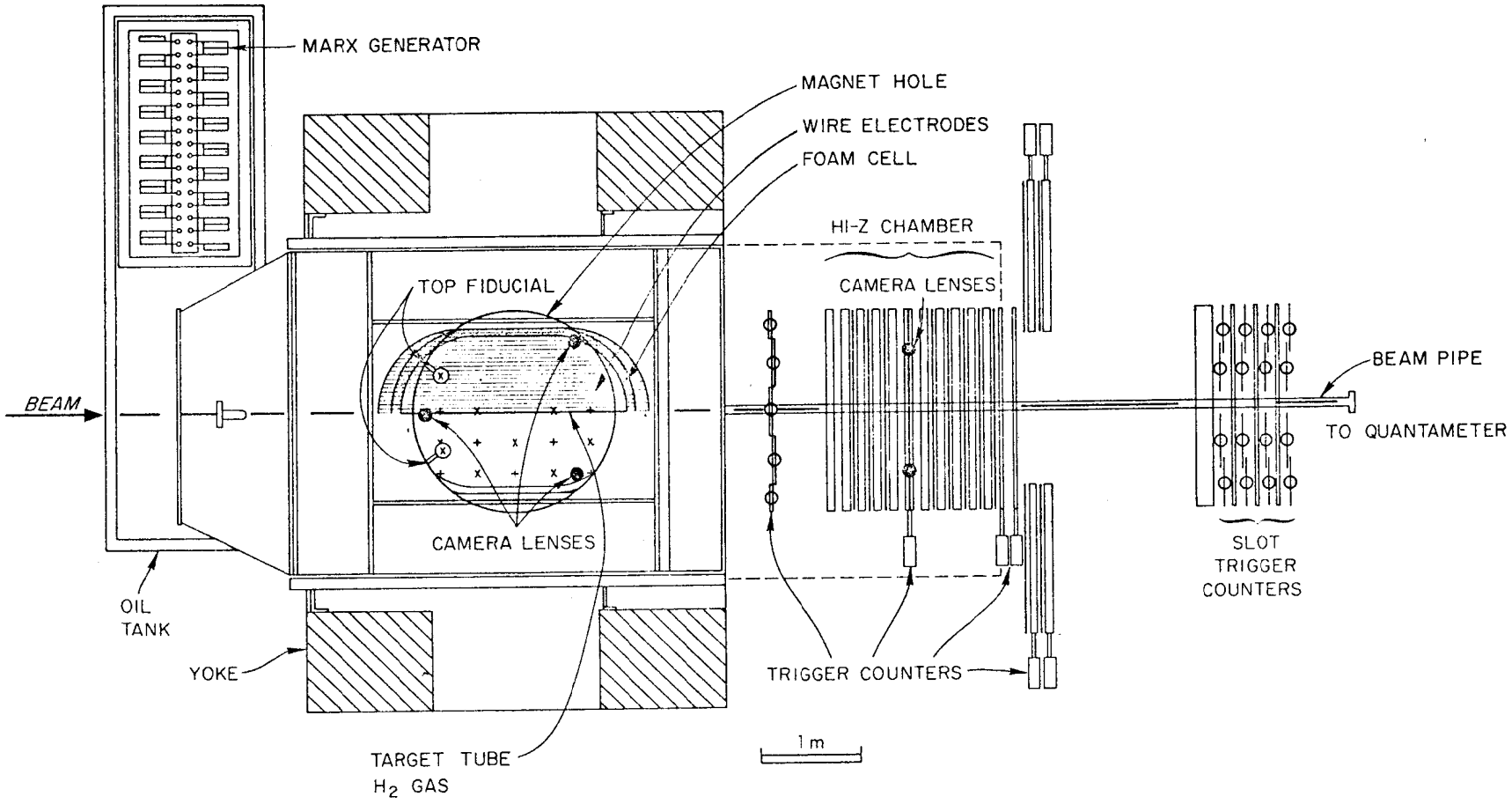
MARX GENERATOR
MAGNET HOLE
WIRE ELECTRODES
FOAM CELL
HI-Z CHAMBER
TOP FIDUCIAL
CAMERA LENSES
BEAM PIPE
BEAM
TO QUANTAMETER
CAMERA LENSES
SLOT
TRIGGER
COUNTERS
OIL
TANK
YOKE
TRIGGER COUNTERS
1 m
TARGET TUBE
H_2 GAS

Fig. 2

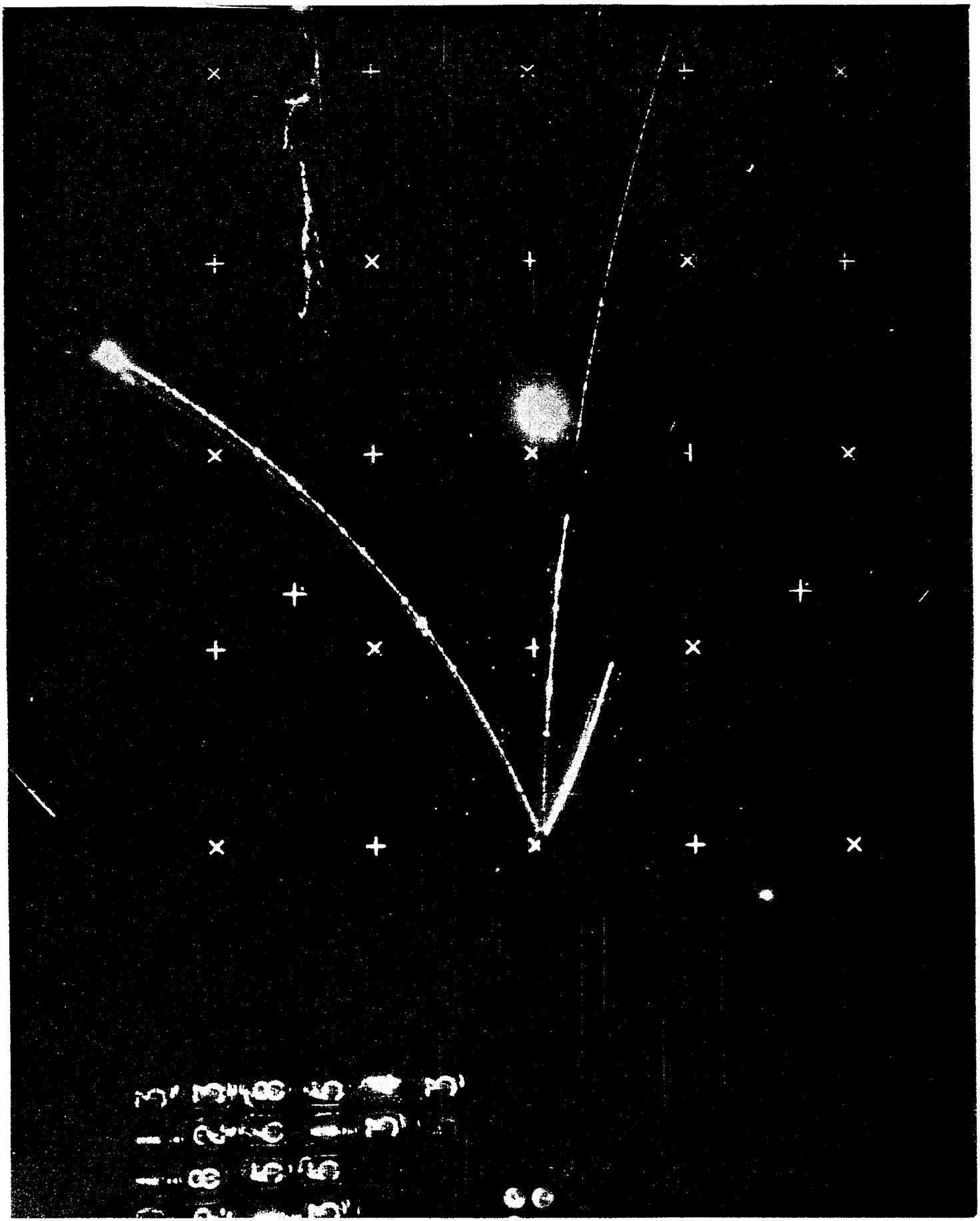

FIG. 3

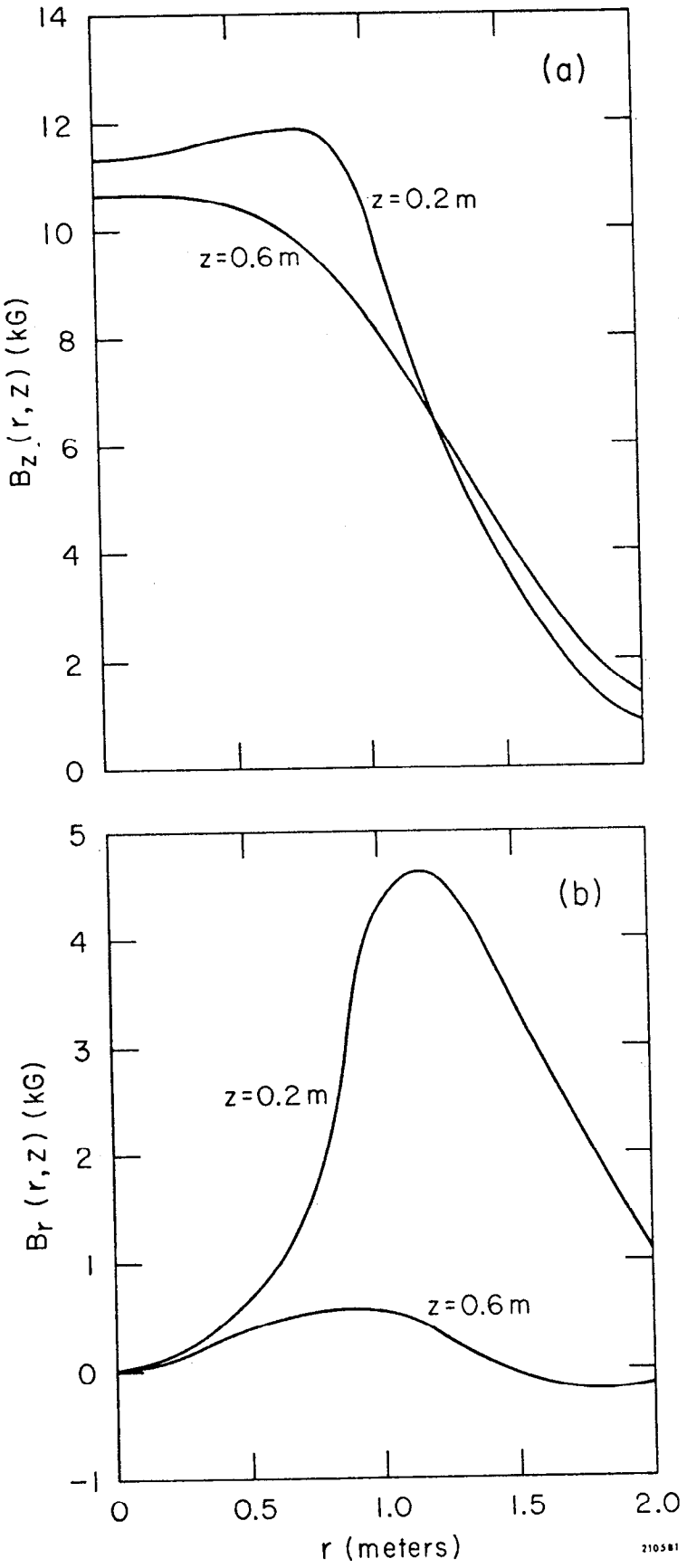
(a)
14
12
10
8
6
4
2
0
B_z (r, z) (kG)
z=0.2 m
z=0.6 m
(b)
5
4
3
2
1
0
−1
B_r (r, z) (kG)
z=0.2 m
z=0.6 m
0
0.5
1.0
1.5
2.0
r (meters)
210581

Fig. 4

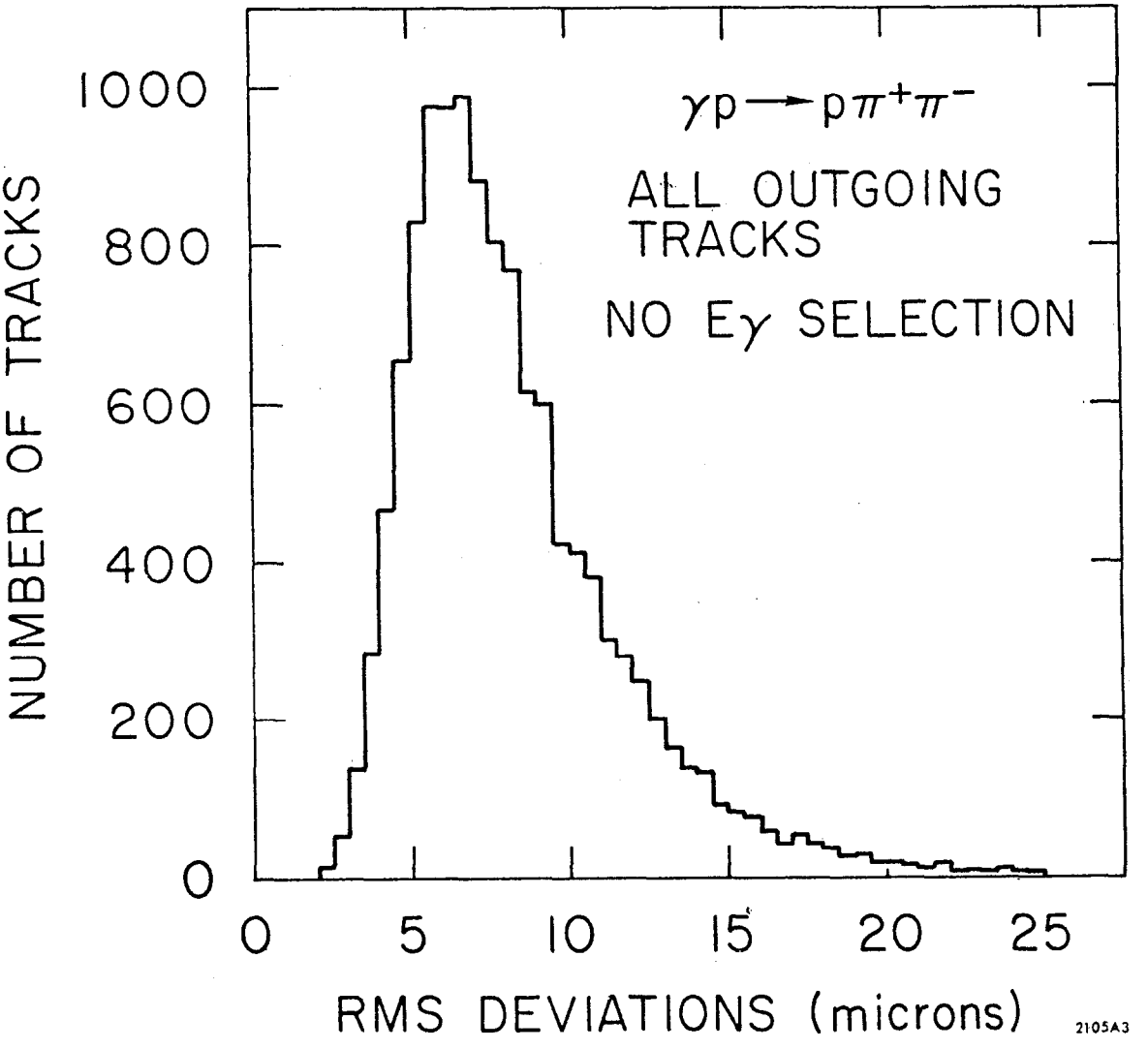
NUMBER OF TRACKS
1000
800
600
400
200
0
0
5
10
15
20
25
RMS DEVIATIONS (microns)
γp → pπ+π−
ALL OUTGOING TRACKS
NO Eγ SELECTION
2105A3

Fig. 5

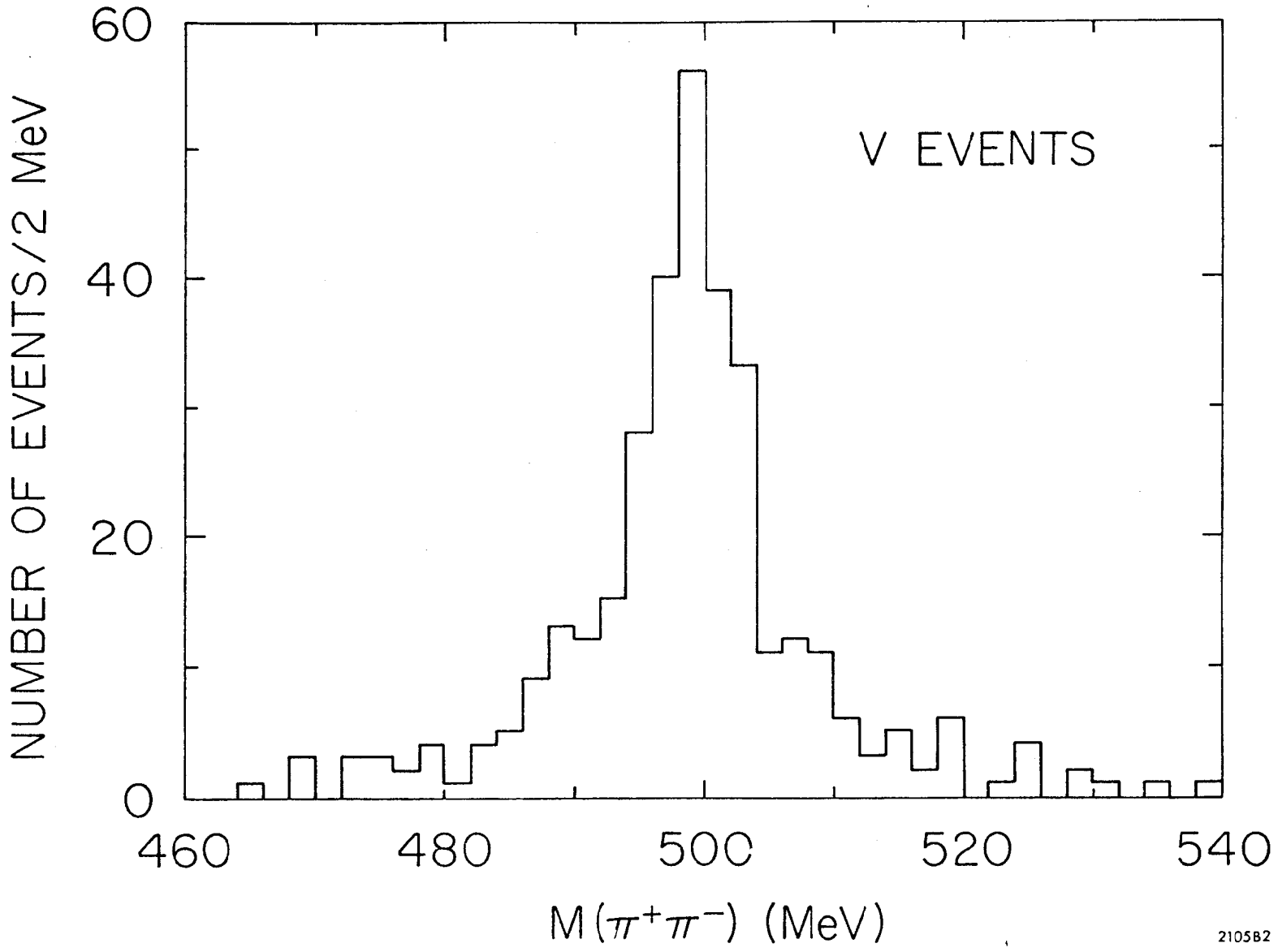
60
40
20
0
NUMBER OF EVENTS/2 MeV
V EVENTS
460
480
500
520
540
M(π+π−) (MeV)
2105B2

Fig. 6

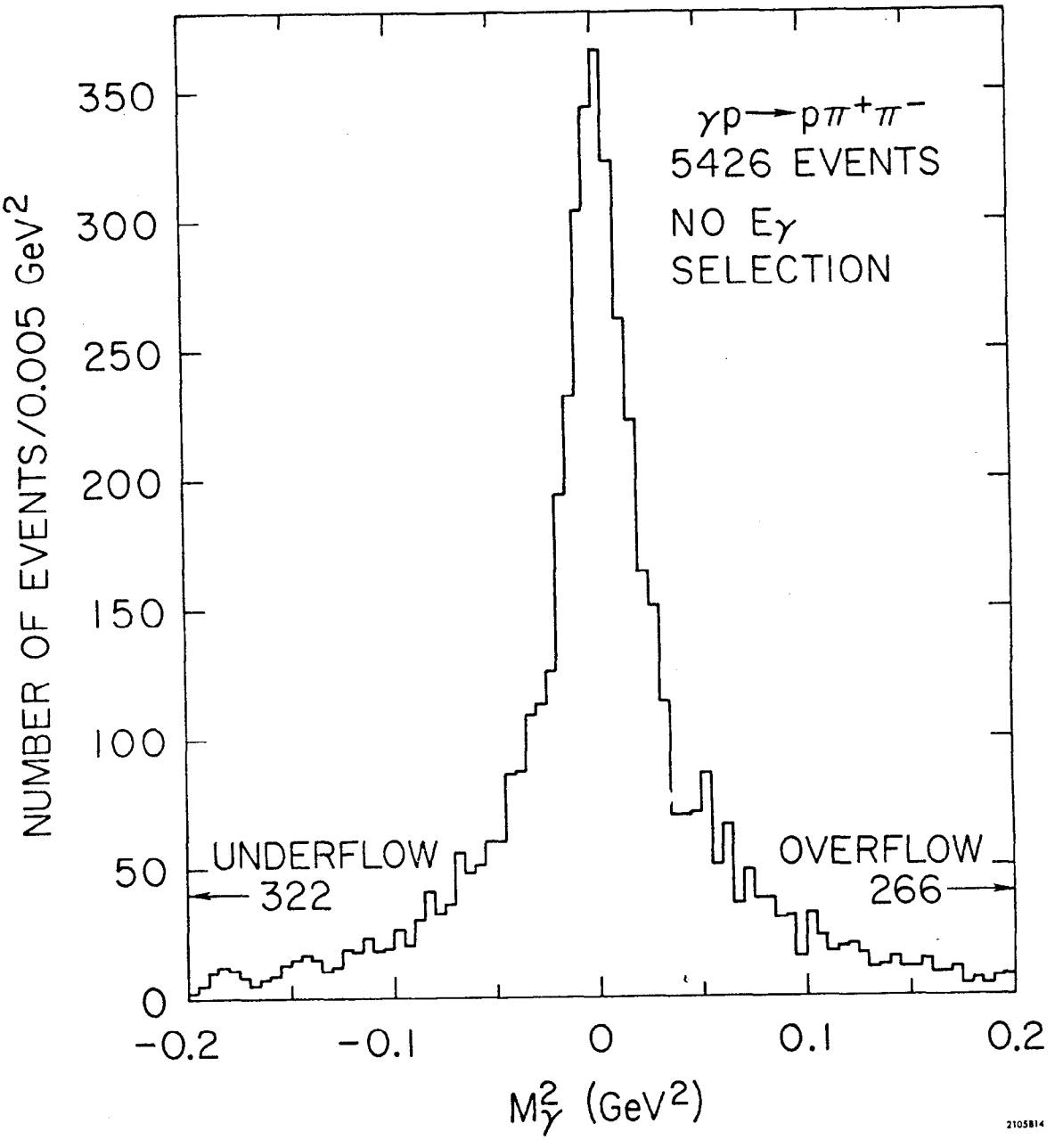
NUMBER OF EVENTS/0.005 GeV^2
350
300
250
200
150
100
50
0
$\gamma p \rightarrow p\pi^+\pi^-$
5426 EVENTS
NO E_γ
SELECTION
UNDERFLOW
322
OVERFLOW
266
-0.2
-0.1
0
0.1
0.2
M^2_{γ} (GeV^2)
2105B14

Fig. 7

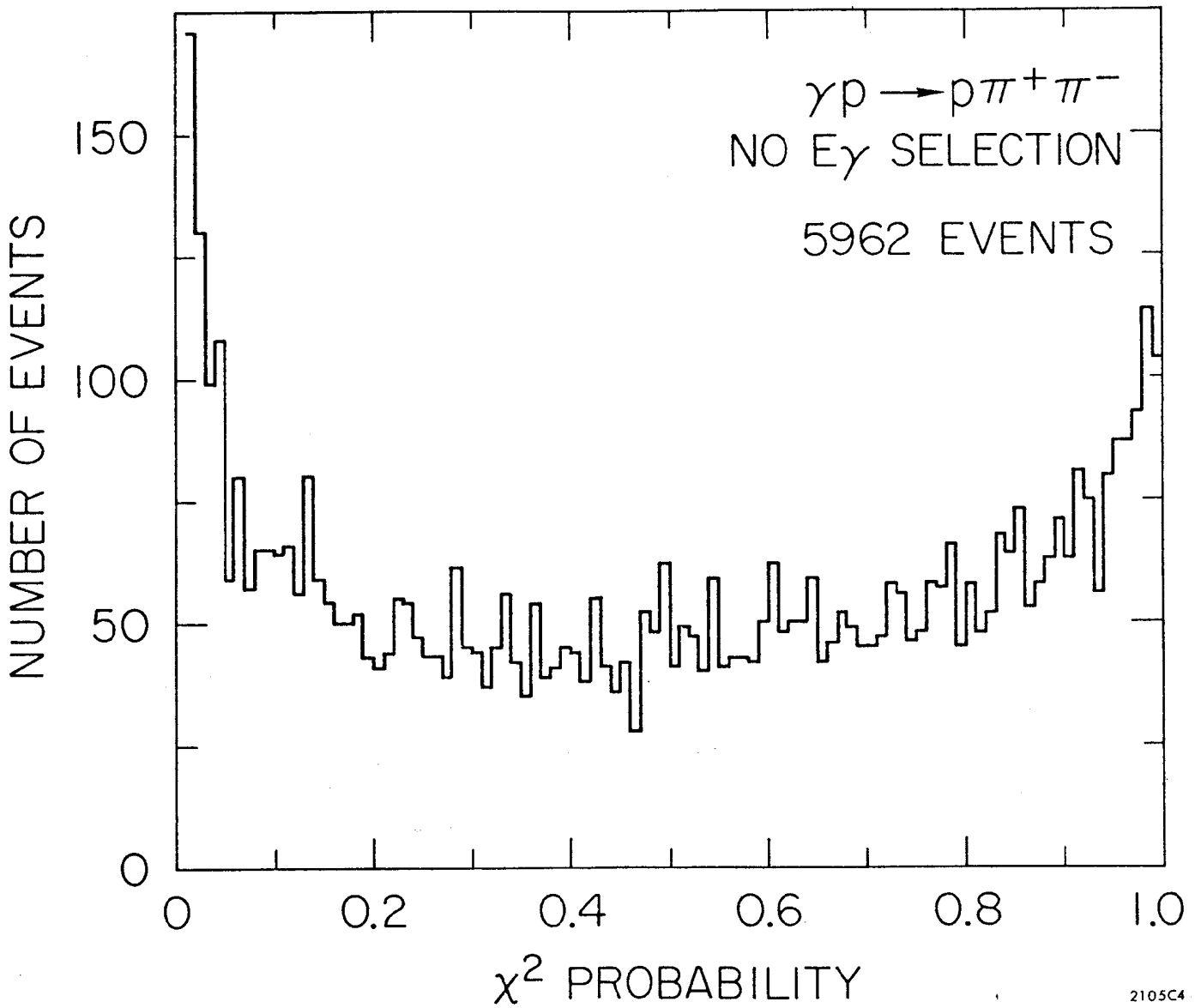
$\gamma p \rightarrow p\pi^+\pi^-$
NO Eγ SELECTION
5962 EVENTS
NUMBER OF EVENTS
150
100
50
0
0
0.2
0.4
0.6
0.8
1.0
χ^2 PROBABILITY
2105C4

Fig. 8

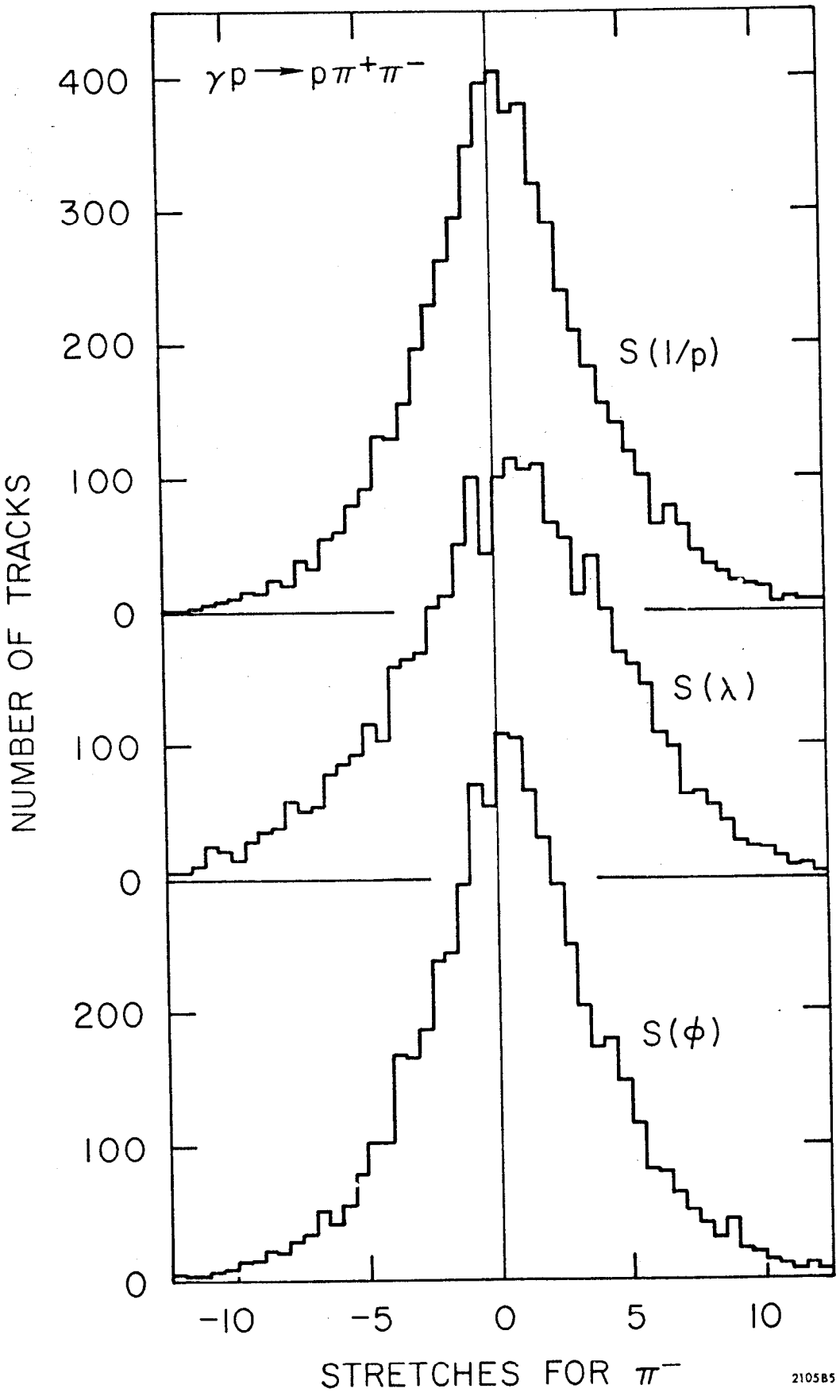
γp → pπ+π−
400
300
200
100
0
S(1/p)
S(λ)
100
0
200
100
0
S(φ)
NUMBER OF TRACKS
−10
−5
0
5
10
STRETCHES FOR π−
2105B5

Fig. 9

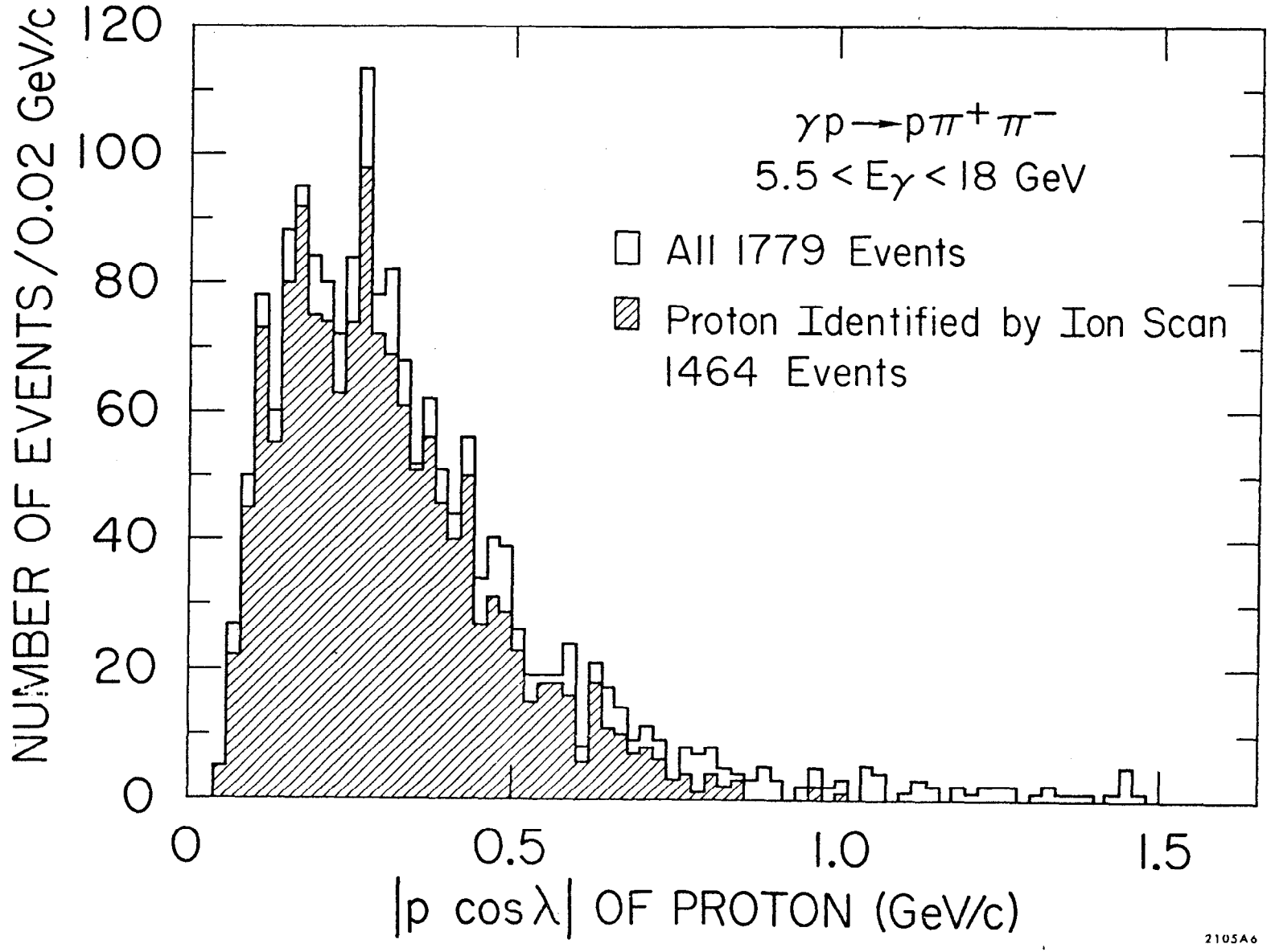
NUMBER OF EVENTS/0.02 GeV/c
120
100
80
60
40
20
0
0
0.5
1.0
1.5
|p cos λ| OF PROTON (GeV/c)
γp→pπ+π−
5.5 < Eγ < 18 GeV
All 1779 Events
Proton Identified by Ion Scan
1464 Events
2105A6

Fig. 10

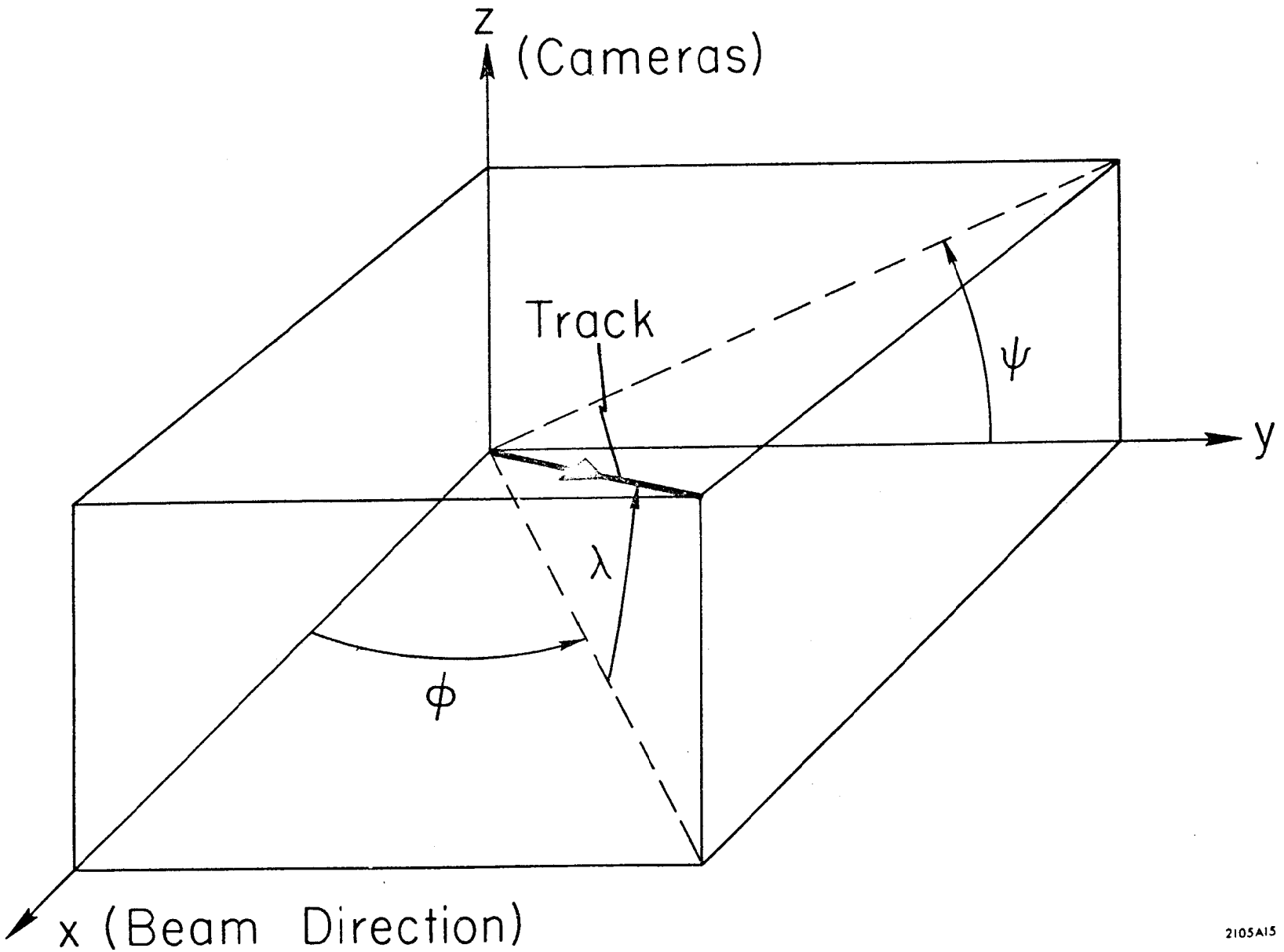

Fig. 11

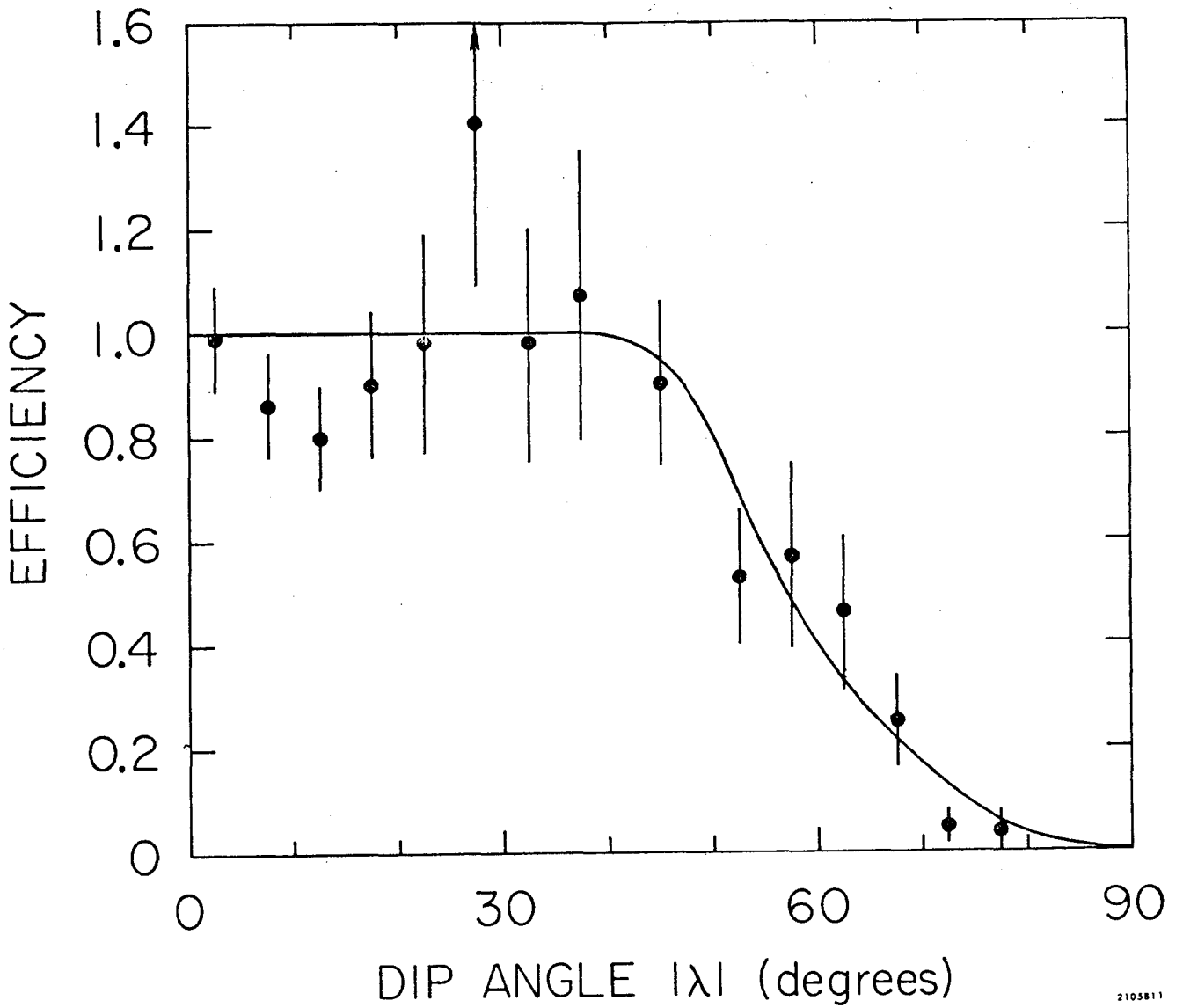
1.6
1.4
1.2
1.0
0.8
0.6
0.4
0.2
0
EFFICIENCY
0
30
60
90
DIP ANGLE |λ| (degrees)
2105811

Fig. 12

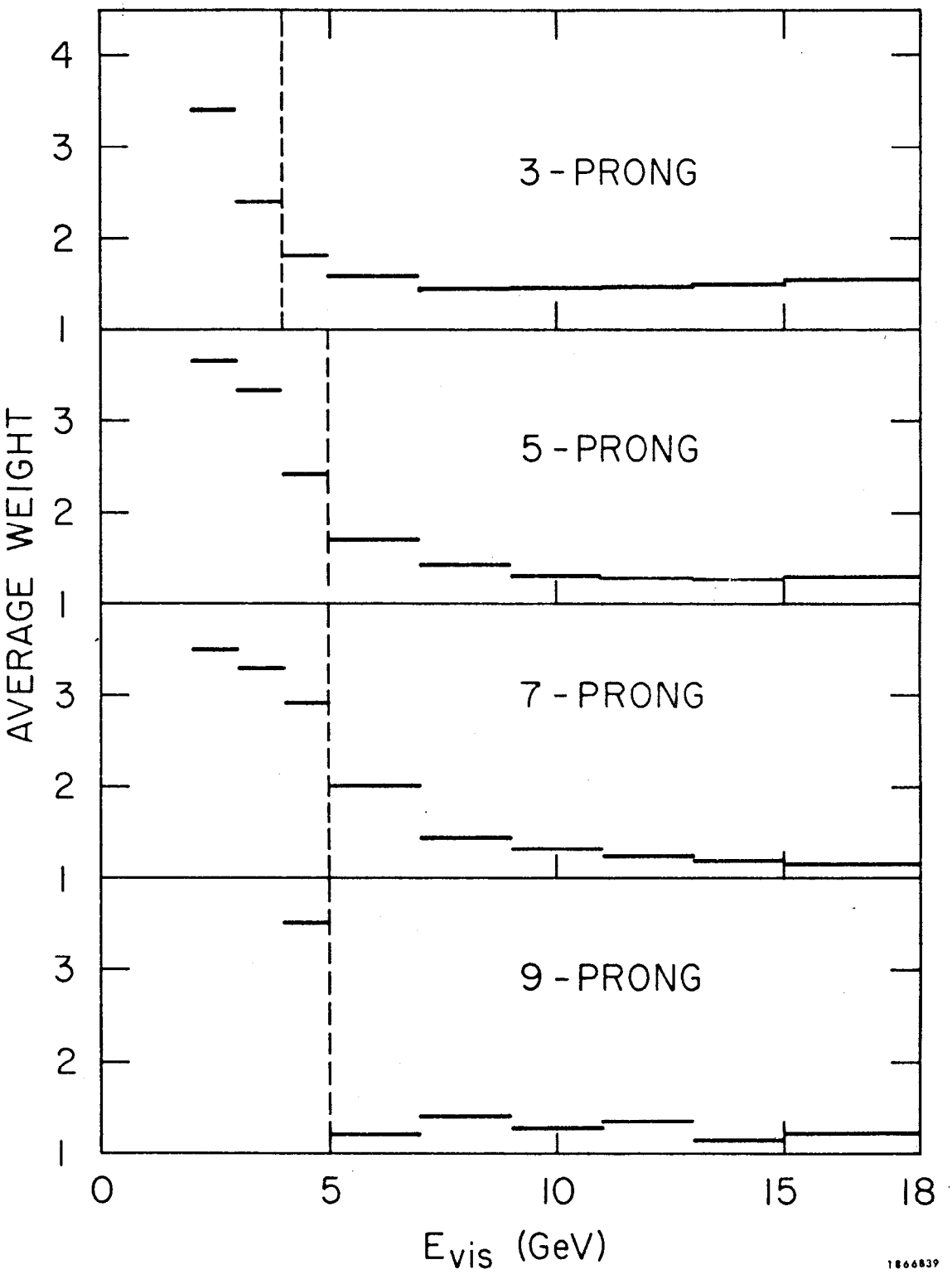
AVERAGE WEIGHT
3 - PRONG
5 - PRONG
7 - PRONG
9 - PRONG
0
5
10
15
18
E_{vis} (GeV)
1866839

Fig. 13

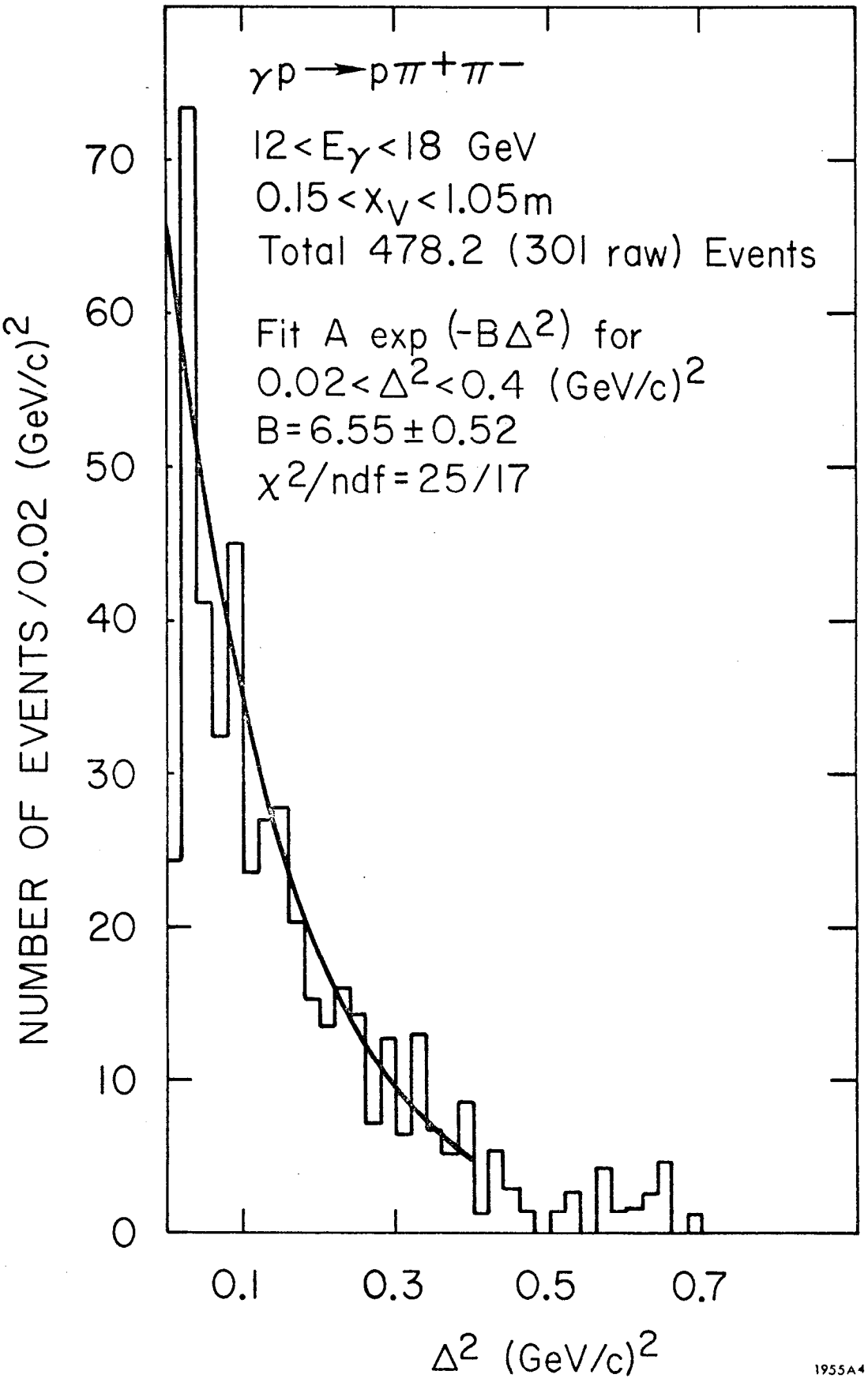
γp → pπ+π−
12<Eγ<18 GeV
0.15<Xv<1.05m
Total 478.2 (301 raw) Events
Fit A exp (-BΔ2) for
0.02<Δ2<0.4 (GeV/c)2
B=6.55±0.52
χ2/ndf=25/17
NUMBER OF EVENTS/0.02 (GeV/c)2
0
10
20
30
40
50
60
70
0.1
0.3
0.5
0.7
Δ2 (GeV/c)2
1955A4

Fig. 14

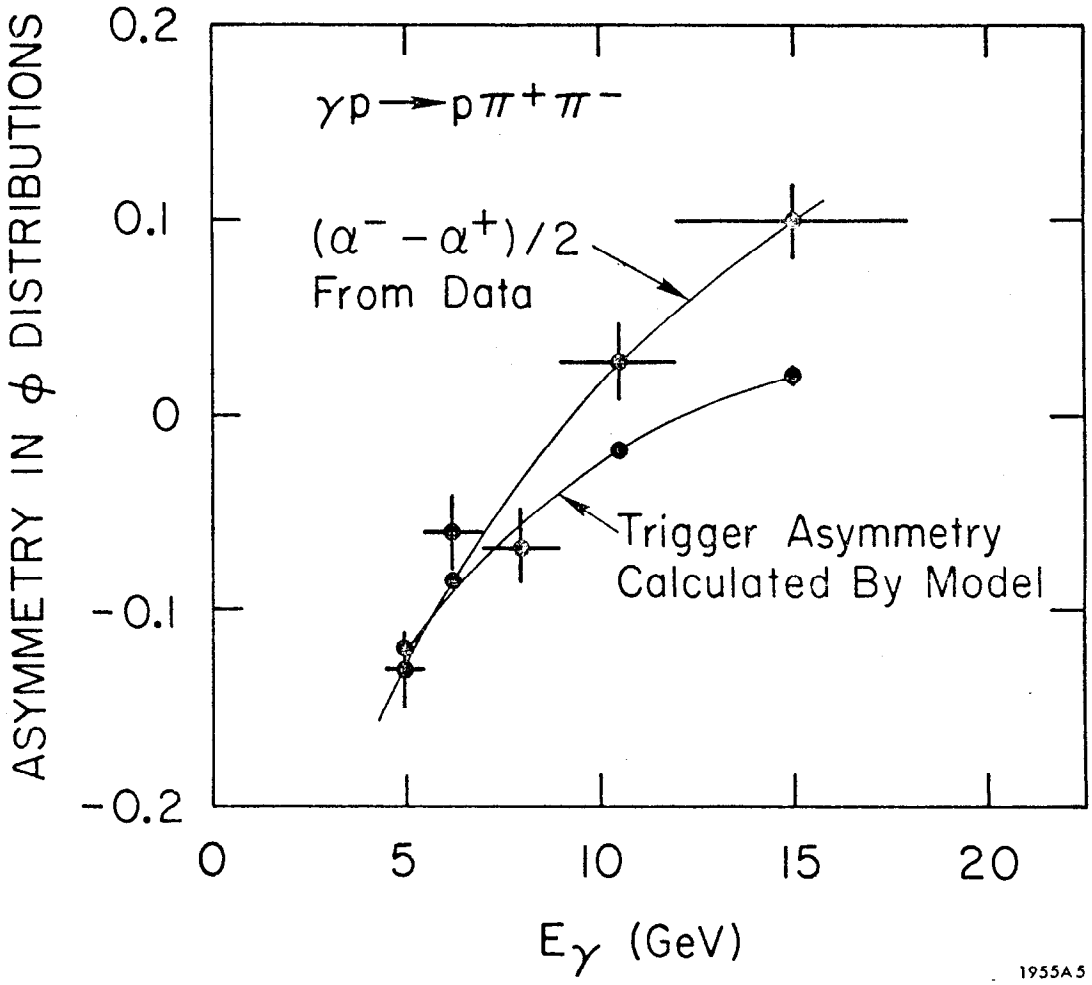
ASYMMETRY IN ϕ DISTRIBUTIONS
0.2
0.1
0
-0.1
-0.2
0
5
10
15
20
E_γ (GeV)
$\gamma p \rightarrow p\pi^+\pi^-$
$(\alpha^- - \alpha^+)/2$
From Data
Trigger Asymmetry
Calculated By Model
1955A5

Fig. 15

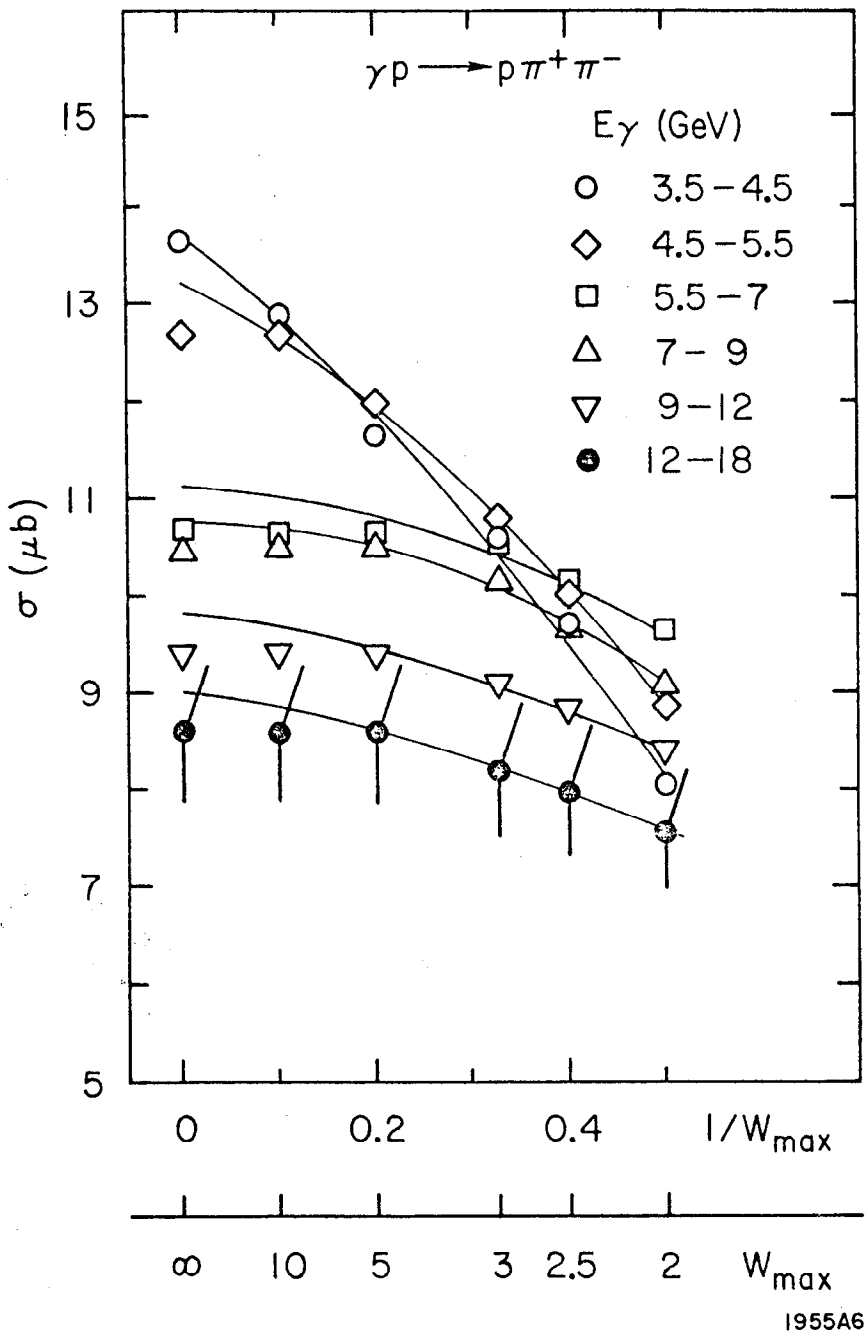
γp ⟶ pπ⁺π⁻
Eγ (GeV)
3.5 – 4.5
4.5 – 5.5
5.5 – 7
7 – 9
9 – 12
12 – 18
σ (μb)
15
13
11
9
7
5
0
0.2
0.4
1/W_max
∞
10
5
3
2.5
2
W_max
1955A6

Fig. 16